Specific primers for real time PCR quantification of *Il7* mRNA were designed using Primer Express software (Applied Biosystems, Forster City CA, USA) and optimized for amplification and minimal primer dimer formations. Primers and probes were designed over a conserved region of the genome and synthesized by Applied Biosystems. Accurate quantification of *Il7* mRNA was accomplished using a plasmid pcDNA3 vector containing the murine *Il7* cDNA (a gift from J. Bream, Johns Hopkins University). DNA sequencing from both the 5′ and 3′ ends verified the identity. The real time PCR assays for *Il7* plasmid DNA/cDNA were carried out in 10 µl reactions using *Il7* specific primers with TaqMan Universal master mix and run on the ABI Prism 7900 (Applied Biosystems, Forster City CA, USA) (50°C for 2 min, 95°C for 10 min followed by 45 cycles at 95°C for 15 sec, 60°C for 30 sec). The murine glyceraldehyde-3-phoshate dehydrogenase (*Gapdh*) plasmid DNA used as a standard was purchased from Serologicals (Gaithersburg, MD, USA). The real time PCR assay for *Gapdh* plasmid DNA was carried out in 10 µl reactions using the murine *Gapdh* control kit (Applied Biosystems) and run as described above. A standard curve was generated by plotting the $\log_{10}$ target dilution, of murine *Gapdh* control template and murine *Il7* on the X-axis against the cycle threshold (C_t) value from serial dilutions (6 log dynamic range) of murine *Gapdh* and *Il7* target DNA on the Y axis. Sensitivity and linear dynamic range were checked on the serial dilutions (10–10^6 copies/reaction) of *Il7* and *Gapdh* plasmid DNA (a standard curve equation $Y = -Mx+b$ is applied to identify the number of molecules of *Gapdh* and *Il7* present in unknown samples). The *Il7* PCR efficiency was 0.968 with a slope of −3.2, while the *Gapdh* PCR efficiency was 0.975 and the slope was −3.3. The *Il7* mRNA expression was then normalized to the *Gapdh* expression values of the same unknown samples to quantify the absolute expression of all samples in the experiment.

Construction of the IL7promECFP mice by BAC recombineering

A bacterial artificial chromosome (BAC) containing the mouse *Il7* gene (RP23-32I7, clone length 228391 bps) was obtained from Invitrogen. BAC DNA was purified using the Nucleobond BAC kit (Clontech) according to manufacturer's instructions and characterized by SpeI fingerprinting.

The construction of the IL7-ECFP-BAC was done using galK selection as described by Warming et al. [50]. Briefly, a *galK* cassette with homology to the first translated exon of *Il7* (exon 1) was amplified using Expand High Fidelity (Roche), pgalK as template, and the following primers (ATG starting site of *Il7* is in bold, sequences priming the pgalK plasmid are underlined):

IL7->galK F: 5′-CCT GCT GCA GTC CCA GTC ATC ATG ACT ACA CCC ACC TCC CGC AGA CCA **TGC** CTG TTG ACA ATT AAT CAT CGG CA-3′ and IL7->galK R: 5′-TCC CCG GCG CGC TAG GCG CAC CTA CTT GTG CGC ACC AGA GAG CAG CGC TTT CAG CAC TGT CCT GCT CCT T-3′. PCR conditions were 94°C 15 sec, 60°C 30 sec and 72°C 1 min for 25 cycles. The PCR reaction was treated with DpnI and gel purified. Purified PCR product was transformed into heat-shocked and electrocompetent SW102 containing RP23-32I7 and Gal^+ colonies were selected as described. Insertion of *galK* resulted in a deletion of the remainder of exon 1 as well as deletion of the splice donor of intron 1. Next, the *galK* cassette was replaced with a PCR product containing homology arms identical to the homology arms used in the first step, amplified from pECFP-1 (Clontech) using the following primers and PCR conditions as described above: galK->ECFP F: 5′-CCT GCT GCA GTC CCA GTC ATC ATG ACT ACA CCC ACC TCC CGC AGA CCA **TGG** TGA GCA AGG GCG AGG A-3′ and galK->ECFP R: 5′-TCC CCG GCG CGC TAG GCG CAC CTA CTT GTG CGC ACC AGA GAG CAG CGC TTG CCT TAA GAT ACA TTG ATG AGT TTG GA. This PCR reaction product was DpnI-treated, gel-purified, and transformed into SW102 Gal^+ cells and DOG resistant colonies were selected as described [50]. One out of 10 analyzed BAC clones was correctly targeted after galK counter selection, and the modified area of the BAC was confirmed by direct BAC sequencing of large-prep BAC DNA using ABI PRISM BigDye Terminators (Applied Biosystems). The IL-7-ECFP BAC construct was linearized with PiSceI (New England Biolabs) and microinjected into fertilized ova of C57BL/6 females at the pronuclear stage. Mice were screened for acquisition of the transgene by Southern Blot Analysis of DNA obtained from tail biopsies using standard procedures. Genomic DNA was digested with BglII and analyzed with a 299 bp probe amplified from the RP23-32I7 BAC. The wild type band is 2.6 kb and the transgenic band is 3.6 kb.

Genotyping and selection of homozygous IL7promECFP transgenic mice

Genomic DNA from mouse tail biopsies was extracted by ethanol precipitation after digestion in digestion buffer (50 mM Tris-HCl, pH 8, 100 mM EDTA, 100 mM NaCl, 1% SDS) with 500 µg Proteinase K (Roche Applied Science, Indianapolis, IN, USA) overnight at 55°C and resuspended in 100 µl of 0.1X SSC buffer. Approximately 10 ng of this DNA was analyzed in a 20 µl SYBR green PCR reaction containing 1X Brilliant SYBR Green QPCR Master Mix (Stratagene), 30 nM ROX passive reference dye, and 300 nM each primer. The ECFP transgene was assayed using specific primers, and differences in input DNA were normalized using an endogenous reference gene, *Folh1*, in separate wells. Primer sequences used were CFP-F 5′-ATG CCA CCT ACG GCA AGC TG-3′, CFP-R 5′-TTC TGC TGG TAG TGG TCG GCG-3′, FolH1-F 5′-CCA AGC AGC CAC AAC AAG TA-3′ and FolH1-R 5′-TCC ATA GGG ATT TTG TGA TTC TG-3′. Real time PCR was performed in triplicate on a MX3000P Stratagene (Cedar Creek, TX, USA) instrument running an initial enzyme activating step of 95°C for 10 min, followed by 45 cycles of denaturation at 95°C for 30 sec, annealing at 60°C for 30 sec, and extension at 72°C for 30 sec. Normalized data was then analyzed using the $-2^{\Delta\Delta Ct}$ method to determine relative fold change compared against a known hemizygous animal (calibrator).

Immunohistochemistry and immunohistology

All tissue samples were fixed in 4% PFA for approximately 16 hrs at 4°C, then transferred to 20% sucrose and incubated for another 16 hrs at 4°C. Finally, tissues were blotted to remove excess sucrose, frozen into OCT compound (Sakura, 4583), and held at −80°C until sectioning. Seven µm sections were cut using a cryostat and stored at −80°C until the day of staining.

For IL-7 immunohistochemistry, sections were warmed to room temperature for approximately 60 min, then rinsed in 1X PBS for 3 changes, 3 min each. Antigen retrieval was performed using a citrate based buffer pH 6 (Biogenex, HK086-9K) in Milestone RHS-1 microwave processor for 10 min to reach 100°C, followed by 10 min at 100°C. Peroxide block was applied at 0.6% in 0.1% saponin (Sigma, S4521)/1X PBS (wash buffer) at room temperature for 15 min followed by rinsing in wash buffer 3 times, 3 min each. Anti-mouse IL-7 antibodies (rabbit polyclonal IgG from Santa Cruz, goat polyclonal IgG from Santa Cruz and R&D, monoclonal rat IgG_{2b} from R&D, biotinylated rabbit polyclonal IgG from PeproTech, monoclonal mouse IgG from Amgen) were applied at different dilutions, in wash buffer, at room temperature

for at least 60 min. Samples were then rinsed using wash buffer 3 times, 3 min each. Avidin-Biotin Complex reagent was applied (ABC, Vector) following manufacturer's instructions diluted in wash buffer, and incubated at room temperature for 30 min, followed by another rinse for 3 times, 3 min each with 1X PBS. Slides were then developed in DAB (Sigma, D5905-100TAB), counterstained, dehydrated, and cover slipped.

For ECFP-target cell identification and co-localization, tissue sections were warmed to room temperature for approximately 60 min, placed in acetone for 10 min at room temperature, and then dried at room temperature for approximately 5 min. Sections were re-hydrated in 1X PBS for 10 min followed by application of 2% normal goat serum/PBS (Vector, S-1000) for 20 min at room temperature. Serum in excess was removed (not rinsed) and primary antibodies were applied for 60 min at 37°C (unless differently specified) as a cocktail diluted in 0.1% BSA/1X PBS. For examining ECFP expression, anti-GFP (Abcam) was used at a 1:1000 dilution. Other antibodies were used at the following dilutions: FITC-anti-Ly51 (BD Pharmingen) at 1:1000; anti-G8.8a (gift from Gray D.) at 1:1000; anti-MTS-15 (gift from Gray D.) 1:20; biotinylated-CD45.2 (eBioscience) at 1:500; FITC-CD11c at 1:1000; CD31 (Santa Cruz) at 1:200 O/N at 4°C. The sections were then rinsed in 1X PBS for 10 min and corresponding secondary antibodies were applied as a cocktail, diluted 1:300 in 1% BSA/1X PBS, for 30 min at room temperature. The following secondary antibodies have been used: donkey anti-rabbit 488 (Molecular Probes), goat anti-rabbit 546, and biotinylated goat anti-rabbit (Vector) followed by streptavidin conjugated Alexa 546 (Molecular Probes) for anti-GFP; goat anti-rabbit 488 (Molecular Probes) for G8.8a; goat anti-rat 546 (Molecular Probes) for MTS-15; streptavidin conjugated Alexa 546 (Molecular Probes) for CD45.2; donkey anti-goat 546 (Molecular Probes) for CD31. Slides were rinsed in 1X PBS for 10 min, wiped dry, and cover slipped with Prolong Gold (Molecular Probes).

All samples were visualized with a Nikon Eclipse 80i microscope under consistent illumination and exposure conditions for each respective stain. Brightfield images were captured using Nikon DXM1200F digital camera and Nikon ACT-1 software. Fluorescent images were obtained using Exfo X-Cite 120 excitation, Nikon UV-2E/C, B-2E/C and G-2E/C filter cubes, Qimaging Retiga 2000R digital camera, and Media Cybernetics Image-Pro plus v5.1 software.

For anti-keratin staining, intact thymic lobes were fixed by immersion in 4% PFA, cryoprotected with phosphate buffered saline containing 30% (w/v) sucrose. Samples were then embedded in OCT (Sakura Finetek U.S.A., Inc., Torrance, CA, USA), frozen, and then sectioned at 5–7 μm with a cryostat. Sections were collected on SuperfrostPlus slides (Fisher Scientific, Pittsburg, PA, USA). After drying overnight, sections were hydrated in PBS and then incubated in a mixture of primary antibodies. To Troma1 hybridoma supernatant (Developmental Studies Hybridoma Bank, University of Iowa; dshb.biology.uiowa.edu/), was added goat anti-green fluorescent protein (Rockland, Gilbertsville, PA, USA), and different rabbit antibodies, either anti-keratin 5, anti-keratin-8 or anti-keratin 14 (all from Covance, Berkley, CA, USA). Controls consisted of mixtures of normal goat, rabbit, and rat IgGs diluted to equivalent concentration. Primary antibodies were applied for 1 hr at room temperature. After repeated washes in PBS, slides were incubated with a mixture of conjugated secondary antibodies diluted in PBS containing 10 mg/ml bovine serum albumin and 10% (v/v) normal donkey serum. Secondary antibodies were donkey anti-goat IgG Alexa 488, donkey anti-rabbit IgG Alexa 555, and chicken anti rat IgG Alexa 647 (all from Invitrogen-Molecular Probes, Eugene, OR, USA). Following incubation for 1 hr. protected from light, the slides were repeatedly washed with PBS, then incubated in 10 mM acetate buffer, pH 6, containing 1 mM $CuSO_4$ for 10 min before a final wash in PBS. Coverslips were mounted with Fluoromount G (SouthernBiotech, Birmingham, AL, USA). Sections were viewed with a Leica microscope equipped with a digital camera (Orca-ER, Hamamatsu Photonic Systems, Bridgewater, NJ, USA) to collect images. Resulting monochrome images were converted to RGB images with Photoshop (Adobe, San Jose CA, USA).

Intravital multiphoton microscopy

Lymphocytes were isolated from OT-IxRAG$^{-/-}$ mice and differentiated into central memory T-cells (TCMs) by stimulation with OVA peptide (SIINFEKL, a generous gift T.Mitchell, U.Louisville) followed by culture in the presence of IL-15 for 5 to 7 days [38]. Differentiation of cells into TCMs was evaluated by FACS analysis for CD8, CD44, CD62L, CD122 and CCR7 expression. Intravital microscopy of mouse bone marrow was performed using a protocol modified from a previous report [38]. Twenty-four hrs after i.v. injection of CFSE-labeled TCMs, mice were anesthetized with isoflurane (Baxter, 2.5% vaporized in an 80:20 mixture of O_2 and air), and the hair in the neck and scalp was removed with hair removal lotion (Nair, Carter Products, NY). The frontoparietal skull was exposed and the mouse head was immobilized in a custom stereotactic holder. The imaging system was an LSM510 NLO Meta (Carl Zeiss, Jena, Germany) driven by a Chameleon femtosecond pulsed laser (Coherent Inc., Santa Clara, CA) tuned to 880 nm, and an inverted microscope (Axiovert 200; Carl Zeiss) equipped with a 40X water immersion objective (Achroplan IR, NA 0.8; Carl Zeiss). The microscope was enclosed in an environmental chamber in which anesthetized mice were warmed by heated air. Fluorescent cells were detected using a bandpass emission filter at 480/40 nm (for ECFP) or 525/50 nm (for CFSE). Vessels were visualized after i.v. injection of 70 kDa Texas Red conjugated-dextran (620/60 nm filter). Image stacks were collected with a 3 μm vertical step size at a depth of 100–150 μm below the skull bone surface. For 3D videos, 4 sequential image stacks were acquired at 3 mm z spacing to cover a volume of 154 μm×154 μm×9.0 μm with a 1 min interval between repetitive image stack collections. Imaging data were processed with Imaris (Bitplane, Zurich, Switzerland).

Supporting Information

Figure S1 Map of BAC used to generate transgenic mice. This BAC was selected because the Il7 gene was flanked by large spans that were likely to contain the regulatory elements.
Found at: doi:10.1371/journal.pone.0007637.s001 (0.10 MB TIF)

Figure S2 No IL-7 expression in non-epithelial cells in thymus. IL-7 is not expressed by myeloid-derived cells, dendritic cells, fibroblasts or endothelial cells in thymus since no co-localization of ECFP (red) with CD45.2, CD11c, MTS-15 or CD31, respectively (green) was observed. DAPI (blue) identifies cell nuclei. Magnification 100X.
Found at: doi:10.1371/journal.pone.0007637.s002 (6.02 MB TIF)

Figure S3 OT-1-TCM migration to bone marrow: Lack of effect of CXCR4 block or Il7 deletion. Central memory cells were generated by in vitro culture of OT-1 cells as described. Cells were labeled with CFSE and injected into wild type mice that were previously injected with HBSS (as a control) or with the CXCR4 antagonist AMD3100 and compared with IL-7−/− recipients.

Twenty-four hours later, bone marrow was harvested from the long bones, stained with anti-CD8 and analyzed by flow cytometry. A. Three individual recipients are shown for each treatment. No inhibition of migration of OT-1-TCM cells resulted from blocking CXCR4 or deleting Il7. Note that the IL-7−/− recipient lacked endogenous CD8 cells. B. The data is shown in numerical form representing the total number of OT-1-TCM cells recovered per individual mouse.
Found at: doi:10.1371/journal.pone.0007637.s003 (1.14 MB TIF)

Table S1 OT-1-TCM association with ECFP producers. Data are corrected by removing OT-1 whose center overlies a stromal cell (probable spill-over artifact).
Found at: doi:10.1371/journal.pone.0007637.s004 (0.03 MB DOC)

Movie S1 Central memory cells (TCMs) were obtained by in vitro differentiation of T cells from OT-1xRAG−/− mice. TCMs were labeled with CFSE and injected intravenously twice (−24 hr and −2 hr) into IL7promECFP mice. Bone marrow was visualized by intravital microscopy. CFSE labeled TCMs (green) exit the blood stream (red) and some interactions with ECFP producing cells (blue) were observed. The video spans a 40 minute time.
Found at: doi:10.1371/journal.pone.0007637.s005 (3.42 MB AVI)

Movie S2 Central memory cells (TCMs) were obtained by in vitro differentiation of T cells from OT-1xRAG−/− mice. TCMs were labeled with CFSE and injected intravenously twice (−24 hr and −2 hr) into IL7promECFP mice. Bone marrow was visualized by intravital microscopy. CFSE labeled TCMs (green) exit the blood stream (red) and some interactions with ECFP producing cells (blue) were observed. The video spans a 40 minute time.
Found at: doi:10.1371/journal.pone.0007637.s006 (2.82 MB AVI)

Acknowledgments

We thank R. Wyles, J. Waters, L. Scheetz and S. Stull for animal technical assistance; K. Noer. R. Matthai and S. Bauchiero for flow cytometry assistance; F.Klauschen for analysis of bone marrow images; R.L. Boyd for MTS-12 and MTS-15 antibodies and J.J. Oppenheim for comments on the manuscript.

Author Contributions

Conceived and designed the experiments: RIM AVW DWM RNG NAJ NGC SKD. Performed the experiments: RIM SW SML MI MA LF ACW DJS JAH MM JC DN LRS AGF KR. Analyzed the data: RIM WQL MRA AGF SKD. Contributed reagents/materials/analysis tools: DHDG BER. Wrote the paper: RIM SKD.

References

1. Khaled AR, Durum SK (2002) Lymphocide: cytokines and the control of lymphoid homeostasis. Nat Rev Immunol 2: 817–830.
2. Peschon JJ, Morrissey PJ, Grabstein KH, Ramsdell FJ, Maraskovsky E, et al. (1994) Early lymphocyte expansion is severely impaired in interleukin 7 receptor-deficient mice. J Exp Med 180: 1955–1960.
3. von Freeden-Jeffry U, Vieira P, Lucian LA, McNeil T, Burdach SE, et al. (1995) Lymphopenia in interleukin (IL)-7 gene-deleted mice identifies IL-7 as a nonredundant cytokine. J Exp Med 181: 1519–1526.
4. Puel A, Ziegler SF, Buckley RH, Leonard WJ (1998) Defective IL7R expression in T(−)B(+)NK(+) severe combined immunodeficiency. Nat Genet 20: 394–397.
5. Puel A, Leonard WJ (2000) Mutations in the gene for the IL-7 receptor result in T(−)B(+)NK(+) severe combined immunodeficiency disease. Curr Opin Immunol 12: 468–473.
6. Namen AE, Lupton S, Hjerrild K, Wignall J, Mochizuki DY, et al. (1988) Stimulation of B-cell progenitors by cloned murine interleukin-7. Nature 333: 571–573.
7. Goodwin RG, Lupton S, Schmierer A, Hjerrild KJ, Jerzy R, et al. (1989) Human interleukin 7: molecular cloning and growth factor activity on human and murine B-lineage cells. Proc Natl Acad Sci U S A 86: 302–306.
8. Montgomery RA, Dallman MJ (1991) Analysis of cytokine gene expression during fetal thymic ontogeny using the polymerase chain reaction. J Immunol 147: 554–560.
9. Montgomery RA, Dallman MJ (1997) Semi-quantitative polymerase chain reaction analysis of cytokine and cytokine receptor gene expression during thymic ontogeny. Cytokine 9: 717–726.
10. Wiles MV, Ruiz P, Imhof BA (1992) Interleukin-7 expression during mouse thymus development. Eur J Immunol 22: 1037–1042.
11. Murray AM, Simm B, Beagley KW (1998) Cytokine gene expression in murine fetal intestine: potential for extrathymic T cell development. Cytokine 10: 337–345.
12. Gunji Y, Sudo T, Suda J, Yamaguchi Y, Nakauchi H, et al. (1991) Support of early B-cell differentiation in mouse fetal liver by stromal cells and interleukin-7. Blood 77: 2612–2617.
13. Golden-Mason L, Kelly AM, Traynor O, McEntee G, Kelly J, et al. (2001) Expression of interleukin 7 (IL-7) mRNA and protein in the normal adult human liver: implications for extrathymic T cell development. Cytokine 14: 143–151.
14. de Saint-Vis B, Fugier-Vivier I, Massacrier C, Gaillard C, Vanbervliet B, et al. (1998) The cytokine profile expressed by human dendritic cells is dependent on cell subtype and mode of activation. J Immunol 160: 1666–1676.
15. Moore NC, Anderson G, Smith CA, Owen JJ, Jenkinson EJ (1993) Analysis of cytokine gene expression in subpopulations of freshly isolated thymocytes and thymic stromal cells using semiquantitative polymerase chain reaction. Eur J Immunol 23: 922–927.
16. Witte PL, Frantsve LM, Hergott M, Rahbe SM (1993) Cytokine production and heterogeneity of primary stromal cells that support B lymphopoiesis. Eur J Immunol 23: 1809–1817.
17. Heufler C, Topar G, Grasseger A, Stanzl U, Koch F, et al. (1993) Interleukin 7 is produced by murine and human keratinocytes. J Exp Med 178: 1109–1114.
18. Matsue H, Bergstresser PR, Takashima A (1993) Keratinocyte-derived IL-7 serves as a growth factor for dendritic epidermal T cells in mice. J Immunol 151: 6012–6019.
19. Matsue H, Cruz PD, Jr., Bergstresser PR, Takashima A (1993) Profiles of cytokine mRNA expressed by dendritic epidermal T cells in mice. J Invest Dermatol 101: 537–542.
20. Roye O, Delhem N, Trottein F, Remoue F, Nutten S, et al. (1998) Dermal endothelial cells and keratinocytes produce IL-7 in vivo after human Schistosoma mansoni percutaneous infection. J Immunol 161: 4161–4168.
21. Watanabe M, Ueno Y, Yajima T, Iwao Y, Tsuchiya M, et al. (1995) Interleukin 7 is produced by human intestinal epithelial cells and regulates the proliferation of intestinal mucosal lymphocytes. J Clin Invest 95: 2945–2953.
22. Madrigal-Estebas L, McManus R, Byrne B, Lynch S, Doherty DG, et al. (1997) Human small intestinal epithelial cells secrete interleukin-7 and differentially express two different interleukin-7 mRNA Transcripts: implications for extrathymic T-cell differentiation. Hum Immunol 58: 83–90.
23. Kroncke R, Loppnow H, Flad HD, Gerdes J (1996) Human follicular dendritic cells and vascular cells produce interleukin-7: a potential role for interleukin-7 in the germinal center reaction. Eur J Immunol 26: 2541–2544.
24. Sorg RV, McLellan AD, Hock BD, Fearnley DB, Hart DN (1998) Human dendritic cells express functional interleukin-7. Immunobiology 198: 514–526.
25. Soslau G, Morgan DA, Jaffe JS, Brodsky I, Wang Y (1997) Cytokine mRNA expression in human platelets and a megakaryocytic cell line and cytokine modulation of platelet function. Cytokine 9: 405–411.
26. He W, Zhang Y, Deng Y, Kabelitz D (1995) Induction of TCR-gamma delta expression on triple-negative (CD3-4-8-) human thymocytes. Comparative analysis of the effects of IL-4 and IL-7. J Immunol 154: 3726–3731.
27. Zamisch M, Moore-Scott B, Su DM, Lucas PJ, Manley N, et al. (2005) Ontogeny and regulation of IL-7-expressing thymic epithelial cells. J Immunol 174: 60–67.
28. Mertsching E, Burdet C, Ceredig R (1995) IL-7 transgenic mice: analysis of the role of IL-7 in the differentiation of thymocytes in vivo and in vitro. Int Immunol 7: 401–414.
29. Tagaya Y, Bamford RN, DeFilippis AP, Waldmann TA (1996) IL-15: a pleiotropic cytokine with diverse receptor/signaling pathways whose expression is controlled at multiple levels. Immunity 4: 329–336.
30. Takeuchi T, Yamanouchi H, Yue Q, Ohtsuki Y (1998) Epithelial component of lymphoid stroma-rich Warthin's tumour expresses interleukin (IL)-7. Histopathology 32: 383–384.
31. Napolitano LA, Grant RM, Deeks SG, Schmidt D, De Rosa SC, et al. (2001) Increased production of IL-7 accompanies HIV-1-mediated T-cell depletion: implications for T-cell homeostasis. Nat Med 7: 73–79.
32. Funk PE, Stephan RP, Witte PL (1995) Vascular cell adhesion molecule 1-positive reticular cells express interleukin-7 and stem cell factor in the bone marrow. Blood 86: 2661–2671.
33. Tsuda S, Rieke S, Hashimoto Y, Nakauchi H, Takahama Y (1996) Il-7 supports D-J but not V-DJ rearrangement of TCR-beta gene in fetal liver progenitor cells. J Immunol 156: 3233–3242.

34. Kitazawa H, Muegge K, Badolato R, Wang JM, Fogler WE, et al. (1997) IL-7 activates alpha4beta1 integrin in murine thymocytes. J Immunol 159: 2259–2264.
35. Terszowski G, Muller SM, Bleul CC, Blum C, Schirmbeck R, et al. (2006) Evidence for a functional second thymus in mice. Science 312: 284–287.
36. Dooley J, Erickson M, Gillard GO, Farr AG (2006) Cervical thymus in the mouse. J Immunol 176: 6484–6490.
37. Kondrack RM, Harbertson J, Tan JT, McBreen ME, Surh CD, et al. (2003) Interleukin 7 regulates the survival and generation of memory CD4 cells. J Exp Med 198: 1797–1806.
38. Mazo IB, Honczarenko M, Leung H, Cavanagh LL, Bonasio R, et al. (2005) Bone marrow is a major reservoir and site of recruitment for central memory CD8+ T cells. Immunity 22: 259–270.
39. Bradley LM, Haynes L, Swain SL (2005) IL-7: maintaining T-cell memory and achieving homeostasis. Trends Immunol 26: 172–176.
40. Ariel A, Hershkoviz R, Cahalon L, Williams DE, Akiyama SK, et al. (1997) Induction of T cell adhesion to extracellular matrix or endothelial cell ligands by soluble or matrix-bound interleukin-7. Eur J Immunol 27: 2562–2570.
41. Zhu J, Garrett R, Jung Y, Zhang Y, Kim N, et al. (2007) Osteoblasts support B-lymphocyte commitment and differentiation from hematopoietic stem cells. Blood 109: 3706–3712.
42. Schluns KS, Kieper WC, Jameson SC, Lefrancois L (2000) Interleukin-7 mediates the homeostasis of naive and memory CD8 T cells in vivo. Nat Immunol 1: 426–432.
43. Tan JT, Dudl E, LeRoy E, Murray R, Sprent J, et al. (2001) IL-7 is critical for homeostatic proliferation and survival of naive T cells. Proc Natl Acad Sci U S A 98: 8732–8737.
44. Li WQ, Jiang Q, Aleem E, Kaldis P, Khaled AR, et al. (2006) IL-7 promotes T cell proliferation through destabilization of p27Kip1. J Exp Med 203: 573–582.
45. Mazzucchelli R, Durum SK (2007) Interleukin-7 receptor expression: intelligent design. Nat Rev Immunol 7: 144–154.
46. Williams IR, Rawson EA, Manning L, Karaoli T, Rich BE, et al. (1997) IL-7 overexpression in transgenic mouse keratinocytes causes a lymphoproliferative skin disease dominated by intermediate TCR cells: evidence for a hierarchy in IL-7 responsiveness among cutaneous T cells. J Immunol 159: 3044–3056.
47. Mombaerts P, Iacomini J, Johnson RS, Herrup K, Tonegawa S, et al. (1992) RAG-1-deficient mice have no mature B and T lymphocytes. Cell 68: 869–877.
48. Gray DH, Chidgey AP, Boyd RL (2002) Analysis of thymic stromal cell populations using flow cytometry. J Immunol Methods 260: 15–28.
49. Gray DH, Fletcher AL, Hammett M, Seach N, Ueno T, et al. (2008) Unbiased analysis, enrichment and purification of thymic stromal cells 3. J Immunol Methods 329: 56–66.
50. Warming S, Costantino N, Court DL, Jenkins NA, Copeland NG (2005) Simple and highly efficient BAC recombineering using galK selection. Nucleic Acids Res 33: e36.

Published December 6, 2010

JEM

Brief Definitive Report

Chemorepulsion by blood S1P regulates osteoclast precursor mobilization and bone remodeling in vivo

Masaru Ishii,[1,2] Junichi Kikuta,[1] Yutaka Shimazu,[1] Martin Meier-Schellersheim,[3] and Ronald N. Germain[2,3]

[1]Laboratory of Biological Imaging, WPI-Immunology Frontier Research Center, Osaka University, Osaka 565-0871, Japan
[2]Lymphocyte Biology Section, Laboratory of Immunology, and [3]Program in Systems Immunology and Infectious Disease Modeling, National Institute of Allergy and Infectious Diseases, National Institutes of Health, Bethesda, MD 20892

Sphingosine-1-phosphate (S1P), a lipid mediator enriched in blood, controls the dynamic migration of osteoclast (OC) precursors (OPs) between the blood and bone, in part via the S1P receptor 1 (S1PR1) which directs positive chemotaxis toward S1P. We show that OPs also express S1PR2, an S1P receptor which mediates negative chemotaxis (or chemorepulsion). OP-positive chemotaxis is prominent in gradients with low maximal concentrations of S1P, whereas such behavior is minimal in fields with high maximal S1P concentrations. This reverse-directional behavior is caused by S1PR2-mediated chemorepulsion acting to override S1PR1 upgradient motion. S1PR2-deficient mice exhibit moderate osteopetrosis as a result of a decrease in osteoclastic bone resorption, suggesting that S1PR2 contributes to OP localization on the bones mediated by chemorepulsion away from the blood where S1P levels are high. Inhibition of S1PR2 function by the antagonist JTE013 changed the migratory behavior of monocytoid cells, including OPs, and relieved osteoporosis in a mouse model by limiting OP localization and reducing the number of mature OCs attached to the bone surface. Thus, reciprocal regulation of S1P-dependent chemotaxis controls bone remodeling by finely regulating OP localization. This regulatory axis may be promising as a therapeutic target in diseases affecting OC-dependent bone remodeling.

CORRESPONDENCE
Masaru Ishii:
mishii@ifrec.osaka-u.ac.jp
OR
Ronald N. Germain:
rgermain@niaid.nih.gov

Abbreviations used: OC, osteoclast; OP, OC precursor; S1P, sphingosine-1-phosphate; S1PR1, S1P receptor 1.

Osteoclasts (OCs) are a specialized cell subset with bone-resorbing capacity that plays a critical role in normal bone homeostasis (bone remodeling), degrading old bones and facilitating new bone formation by osteoblasts (Teitelbaum, 2000). OCs are differentiated from monocyte/macrophage-lineage hematopoietic precursor cells, termed OC precursors (OPs), and previous studies have revealed key molecular signals, such as those mediated by M-CSF and RANKL, that regulate OC differentiation (Karsenty and Wagner, 2002; Teitelbaum and Ross, 2003). In contrast to the detailed information available concerning molecular signals for differentiation of OC, the factors controlling migration and localization of OPs onto the bone surface, the site of OC terminal differentiation, are less well analyzed. We have recently used intravital two-photon microscopy to visualize the bone cavity in live mice, and found that sphingosine-1-phosphate (S1P), a lipid mediator enriched in blood, plays a critical role in controlling the residence stability of OPs on the bone surface via the cognate receptor S1P receptor 1 (S1PR1; also designated $S1P_1$ or Edg-1; Ishii et al., 2009; Klauschen et al., 2009). The mechanisms controlling the initial localization of OPs into the bone space or counteracting the tendency of S1P to promote movement of OPs from bone to blood, however, have not yet been clarified. In this paper, we show that bone attraction is also contributed to in part by S1P, through a distinct but related receptor, S1PR2 (also designated as $S1P_2$ or Edg-5).

Although both S1PR1 and S1PR2 belong to the heptahelical heterotrimeric G protein–coupled Edg receptor family, their signal

The Rockefeller University Press $30.00
J. Exp. Med. Vol. 207 No. 13 2793-2798
www.jem.org/cgi/doi/10.1084/jem.20101474

Supplemental Material can be found at:
http://jem.rupress.org/content/suppl/2010/12/06/jem.20101474.DC1.html

Published December 6, 2010

transduction pathways are completely different (Takuwa, 2002; Rosen and Goetzl, 2005). S1PR1 (via its associated $G_i\alpha$ subunit) activates the small G protein Rac and induces positive chemotaxis. In contrast, S1PR2 (signaling through $G_{12/13}\alpha$) activates another small G protein, Rho. Active Rho can inhibit activation of Rac, which can limit S1P-induced chemotaxis (Fig. 1 A). It was previously reported that S1PR2-expressing cells show reduced migration to S1P in vitro (Okamoto et al., 2000).

RESULTS AND DISCUSSION

We found that OPs express S1PR2 as well as S1PR1, and the positive migratory response to S1P was highly concentration dependent, being more vigorous at low S1P concentrations ($<10^{-7}$ M) and less marked at higher concentrations (Fig. 1 B). In addition, blockade of S1PR1 signaling with pertussis toxin led to a reduction in migration below the basal level seen in the absence of S1P, suggesting that S1P could have a negative effect on cell migration under these conditions. We also found that S1PR2 deficiency enhanced positive S1P chemotaxis. To better analyze the effects of varying S1P concentrations on migration, we examined the dynamics of S1P chemotaxis in an in vitro image-based system (Fig. 1, C and D). In these experiments, cells were applied in the one chamber and S1P was added in the other chamber. In this device, a narrow plateau between the chambers generates a linear gradient experienced by the cells on the opposite side of the chemokine-filled chamber, and the motility of the cells can be assessed throughout

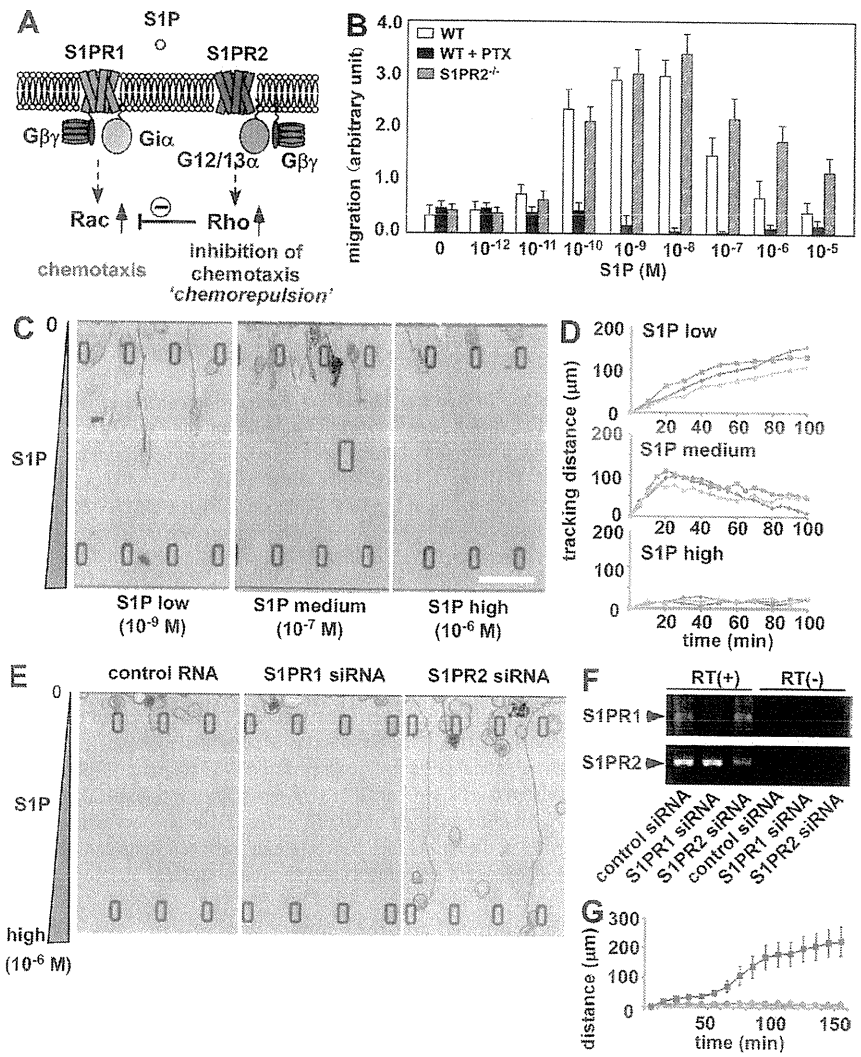

Figure 1. Reciprocal control of S1P chemotaxis by counteracting the receptors S1PR1 and S1PR2. (A) Scheme of function and signal transduction of S1PR1 and S1PR2. (B) In vitro chemotactic response of BM-MDM isolated from wild-type and S1PR2-deficient mice. Before the chemotaxis assay, some cells were treated with 100 nM pertussis toxin (PTX). Error bars represent SD ($n = 6$, from three independent experiments). (C) In vitro S1P-directed chemotaxis of RAW264.7 cells dynamically visualized using EZ-Taxiscan. Cells were loaded in one side of the chamber and the other side was filled with medium containing indicated concentration of S1P (Videos 1–3). Cells migrate into the terrace between the loading chambers. The height from floor to ceiling of the terrace is 8 μm. Bar, 100 μm. (D) Tracking courses from the start line of representative cells in low, medium, and high S1P conditions. Each curve shows the data from one experiment and represents the averaged tracking distance of multiple cells over time. The EZ-Taxiscan experiments were independently performed six times and the data were largely consistent, although the extent of the toward-and-away motions of cells in 10^{-7} M S1P was variable depending on the experiment. Obvious away motion could clearly be observed in five of the six experiments (62 in 83 total cells), and the cells simply stopped in the middle of the chamber without clear backward migration in one of the six experiments (11 in 83 cells). (E) In vitro S1P-directed chemotaxis of RAW264.7 cells treated with siRNAs. Cells pretreated with control RNA duplex, siRNA against S1PR1, or siRNA against S1PR2 (Videos 4–6) were loaded into the EZ-Taxiscan chamber filled with a high concentration of S1P (10^{-9} M) in the other side. (F) RT-PCR detection of S1PR1 and S1PR2 in siRNA-pretreated RAW264.7 cells. Cells were pretreated with control RNA duplex (control siRNA), siRNA against S1PR1 (S1PR1 siRNA), or siRNA against S1PR2 (S1PR2 siRNA). (G) Migration distance data from microscopic analysis of control (red), S1PR1 knockdown (green), and S1PR2 knockdown (blue) cells. The experiments were independently performed three times and the data were largely consistent. Each dot represents the mean value of six independent cells and error bars represent SD.

Published December 6, 2010

their exposure to this chemokine gradient in the imaging chamber. RAW264.7 cells, which are often used as a model of OPs, readily migrated toward a low maximal concentration of S1P (10^{-9} M; Fig. 1, C [left] and D [top]; and Video 1) but not toward a high maximal S1P concentration (10^{-6} M; Fig. 1, C [right] and D [bottom]; and Video 3). Strikingly, at an intermediate concentration, cells first moved up the S1P gradient but then arrested this movement and began to migrate back in the opposite direction in nearly all cases (Fig. 1, C [middle] and D [middle]; and Video 2). These data reveal that at high S1P concentrations, RAW264.7 cells respond by chemorepulsion rather than chemoattraction.

RNA interference was used to examine the roles of S1PR1 and S1PR2 in these S1P concentration-dependent behaviors (Fig. 1, E and G). Cells were treated with siRNAs targeting S1PR1 or S1PR2 and put in a high S1P concentration field (10^{-6} M; Fig. 1, E and F). Although control cells and S1PR1 knockdown cells were hardly motile, as observed in Fig. 1 C (Fig. 1, E [left two panels] and G; and Videos 4 and 5), some of the cells treated with siRNA targeting S1PR2 could migrate vigorously, irrespective of the high S1P concentration (Fig. 1, E [right] and G; and Video 6). We also confirmed that S1PR2-deficient primary cultured OPs can efficiently move toward a high S1P concentration (Fig. S1), establishing that S1PR2 expressed on OPs is indeed functional and that this receptor is responsible for the chemorepulsive behavior of these cells (Fig. 1, B and C). These results clearly demonstrate that OPs express two counteracting receptors for S1P: forward movement, promoting S1PR1, and backward movement, promoting S1PR2. The migratory behavior of OPs is thus finely regulated by the balance of the reciprocal functions of these two receptors and their differential activity at distinct concentrations of S1P.

To investigate whether S1PR2 affects OP migration in vivo as these in vitro studies would imply, we performed intravital two-photon imaging of calvaria bones (Mazo et al., 2005; Ishii et al., 2009) and examined the migratory behavior of monocytoid cells resident in the marrow spaces, including OPs. We used CX_3CR1-EGFP knockin (heterozygous) mice (Jung et al., 2000; Niess et al., 2005), in which monocyte-lineage cell types predominantly expressed EGFP. We have previously confirmed that TRAP (tartrate-resistant acid phosphate)-positive mature OCs expressed EGFP in these animals (Ishii et al., 2009) and, in addition, we confirmed that $EGFP^+$ cells (but not $EGFP^-$) can efficiently differentiate into OC-like cells in vitro upon stimulation with RANKL (Fig. S2). Both of these results strongly suggest that $EGFP^+$ cells contain OPs.

CX_3CR1-EGFP–positive cells present in BM stromal locations or at the bone surface were generally stationary under control conditions (Fig. 2 A, top; and Video 7). In contrast, a subset of the labeled cells became motile 2 h after the intravenous application of 3 mg/kg JTE013 (Osada et al., 2002), a potent antagonist for the S1PR2 receptor (Fig. 2 A, bottom; and Video 8), with some of the mobilized cells entering the blood circulation. The cell-mobilizing effect of JTE013 was

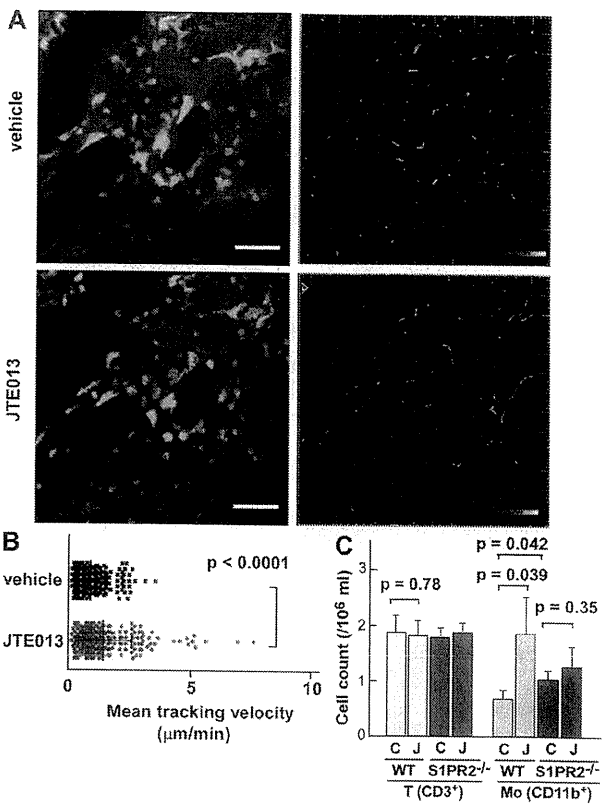

Figure 2. In vivo S1PR2-mediated migration control of OP monocytes visualized using intravital two-photon imaging. (A) Intravital two-photon imaging of mouse skull bone tissues of heterozygous CX_3CR1-EGFP knockin mice, in the absence (vehicle; Video 7) or presence (Video 8) of 3 mg/kg of the S1PR2 antagonist JTE013. CX_3CR1-EGFP–positive cells appear green. The microvasculature was visualized by intravenous injection of 70 kD dextran-conjugated Texas red (red; left). The movements of CX_3CR1-EGFP–positive cells were tracked for 10 min (right). Colored lines show the associated trajectories of cells. Bars, 50 μm. (B) Summary of mean velocity of CX_3CR1-EGFP–positive cells treated with JTE (red circle) or vehicle (blue square). Data points (n = 252 for vehicle and n = 237 for JTE013) represent individual cells compiled from six independent experiments, and error bars represent SD. (C) Effect of the S1PR2 antagonist JTE013 on the composition of peripheral mononuclear cells. Peripheral mononuclear cells collected from wild-type and $S1PR2^{-/-}$ mice administered vehicle (C) or JTE013 (J) were stained with anti-CD3 or anti-CD11b. Absolute numbers of $CD3^+$ T cells or $CD11b^+$ monocytoid cells are described in the figure. Each bar represents the mean value derived from three independent experiments and error bars represent SD.

less pronounced and took longer than was the case with the S1PR1 agonist SEW2871 (Ishii et al., 2009), although the effect was statistically significant (Fig. 2 B). Data collected using larger imaging fields revealed that there was a significant heterogeneity in cellular dynamics that correlated with location of the cells within the BM cavity (Fig. S2 and Video 9). CX_3CR1-$EGFP^+$ cells positioned at the bone surface hardly move, suggesting that these cells have already committed to OC differentiation. In contrast, cells in the parenchyma move after application of JTE013 and, more importantly, the migratory

Published December 6, 2010

activities of cells around sinusoids are significantly higher than those of cells in the parenchyma around large collecting venules. Together, these findings suggest that sinusoids are the plausible locations for mobilization of these cells.

Consistent with these findings, we also observed an elevated percentage and absolute number of monocytoid cells in peripheral blood from JTE013-treated mice (Fig. 2 C). This phenomenon was largely absent in S1PR2-deficient mice, suggesting that the effect of JTE013 is exclusively mediated by S1PR2. These results are consistent with the idea that an S1PR2 antagonist can block OP chemorepulsion mediated by the high S1P concentration in blood vessels, facilitating the recirculation of OPs.

To evaluate the in vivo impact of such S1PR2-mediated chemorepulsion of OPs on bone remodeling, we examined mice deficient in S1PR2 (Kono et al., 2004). Morphohistometric analyses using μCT showed that femora of mice genotyped as S1PR2 were moderately osteopetrotic, compared with those of control littermates (Fig. 3 A). Bone tissue density (Fig. 3 B, B.V./T.V.) of S1PR2$^{-/-}$ mice was significantly higher than that of controls, and concordantly trabecular density (Fig. 3 B, Tb.N.) was increased in S1PR2$^{-/-}$ bones. Conventional bone morphohistometrical analyses demonstrated a significant decrease in osteoclastic bone resorption (Fig. 3 C, E.S./B.S.) in S1PR2$^{-/-}$ bones, whereas osteoblast formation was not significantly affected. These results clearly suggest that OC attachment to and function on the bone surface was impaired in S1PR2$^{-/-}$ animals, leading to reduced bone resorption and moderate osteopetrosis. Because the expression of S1PR2 is high in monocytoid OPs and is hardly detected in osteoblast-lineage cells (unpublished data), and because S1PR2 deficiency did not alter the capacity of OP to differentiate into OCs (Fig. S1), this result indicates that S1PR2-mediated chemorepulsion of OPs in response to the high blood S1P concentration contributes to their localization at the bone surface and promotes osteoclastogenesis in vivo.

This newly revealed role of S1PR2-mediated control of OP migration prompted us to examine their therapeutic implications. i.p. administration of RANKL induces substantial osteoporosis within 2 d (Tomimori et al., 2009). We added daily administration of 3 mg/kg of the S1PR2 antagonist JTE013 to this regimen and examined the effect on bone mineral density (Fig. 3 C). Addition of JTE013 significantly reversed the bone density loss induced by RANKL administration (Fig. 3 C, left) by limiting osteoclastic bone resorption (Fig. 3 C, right, E.S./B.S.). This therapeutic effect of JTE013 was absent in S1PR2-deficient mice, suggesting that the function of JTE013 is dependent on this receptor. We also tested the effect of JTE013 by using ovariectomized mice, a conventional model for postmenopausal osteoporosis, and confirmed the significant therapeutic potentials (Fig. S3).

We have previously shown that the S1P–S1PR1 axis contributes to recirculation of OPs into the blood stream (thus acting as a circulation-attractive factor), whereas bone-attractive factors have not been fully elucidated. In this study,

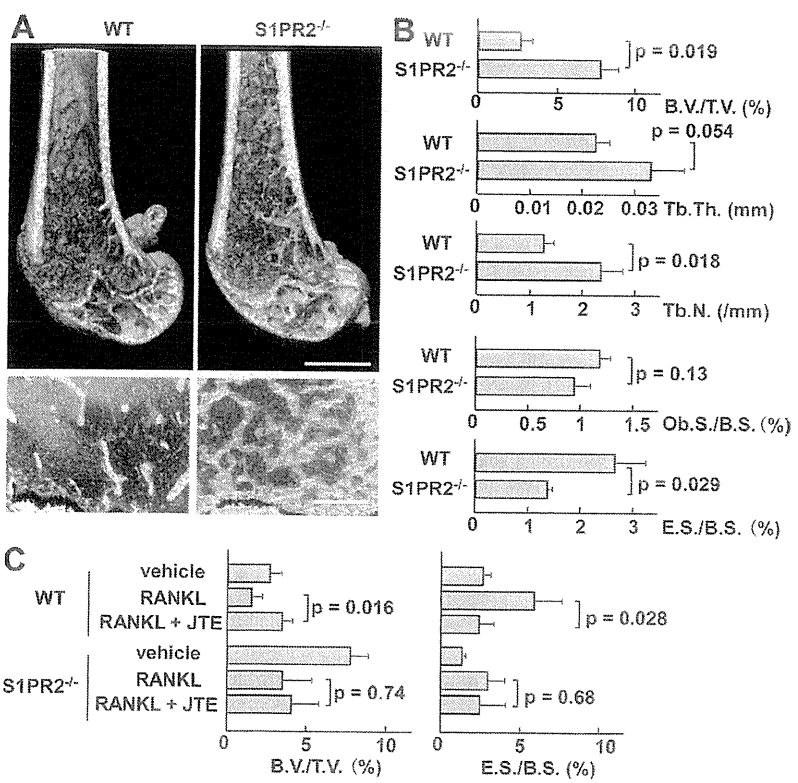

Figure 3. In vivo impact of S1PR2 on bone remodeling. (A) Morphohistometric analyses of control and S1PR2-deficient (S1PR2$^{-/-}$) littermates. Femoral bone samples were analyzed by cone-beam μCT (top) and conventional histological examination (bottom). Bars: (top) 1 mm; (bottom) 200 μm. (B) Summary of the data of bone matrix density (bone volume/tissue volume = B.V./T.V.), trabecular thickness (Tb.Th.), trabecular density (Tb.N.; calculated from μCT images), osteoblast surface per bone surface (Ob.S./B.S.), and osteoclastic erosion surface per bone surface (E.S./B.S.; calculated by conventional morphohistometrical analyses). Error bars represent SD. $n = 3$ for each (from three littermates). (C) Therapeutic effect of S1PR2 antagonist JTE013 on osteoclastic bone resorptive changes. Femurs were collected from each mouse (wild-type and S1PR2$^{-/-}$) after three different treatments: PBS + vehicle, RANKL + vehicle, and RANKL + JTE013. RANKL was dissolved in PBS, and JTE013 was dissolved in a vehicle (PBS containing 5% acidified DMSO and 3% fatty acid–free BSA). Mice were i.p. injected with PBS or RANKL, and with JTE or vehicle, every day for 2 d. Bone samples were analyzed by cone-beam μCT and conventional morphohistological examination. Data of bone matrix density (B.V./T.V.) calculated from μCT images (left) and osteoclastic erosion surface per bone surface (E.S./B.S.) calculated by conventional morphohistometrical analyses (right) were shown. Error bars represent SD. $n = 3$ for each (from three littermates).

Published December 6, 2010

we demonstrate a complex regulatory system in which S1P also acts as a bone attractant in certain conditions (actually functioning as a circulation repellant) through a different cognate receptor, S1PR2. In contrast to several chemokines that have already been reported to be important for OP localization, such as CCL2 (Binder et al., 2009), CCL9 (Yang et al., 2006), CXCL1 (Onan et al., 2009), and CXCL12 (Gronthos and Zannettino, 2007), we assume that the S1P–S1PR1/S1PR2 reciprocal axes contribute to regulating the initial entry/exit of OPs across the border of BM vasculature, rather than attachment at the bone surface by itself.

Given these data, we suggest the following model for S1P-mediated localization control of OPs in bone tissues in vivo (Fig. S3). As with other tissues and organs, the S1P concentration in bone tissues is relatively low (Maeda et al., 2010), forming a substantial S1P gradient between BM tissues (parenchyma), the sinusoids, and blood vessels, which is a prerequisite for S1P chemotaxis in situ. Because S1PR1 is readily down-regulated by endocytosis in a high S1P environment, OPs in blood vessels could enter into bones by S1PR2-mediated repulsion, although S1PR2-mediated OP entry into BM has not been fully demonstrated in the present experiments. In addition, we do not assume this is the only mechanism regulating OP entry but rather consider several bone-enriched chemokines, CXCL12 chief among them (Gronthos and Zannettino, 2007), to also be involved in bone recruitment, with S1PR2-mediated chemorepulsion facilitating this process. Once they entered into the parenchyma, S1PR1 would be reexpressed on the cell surface, prompting potential reentry into the circulation if other factors (chemokines and adhesion molecules) at the bone surface do not override this chemoattractive effect. Although it cannot be measured precisely, S1P concentration in BM sinusoids, because of leakage across endothelial barriers, might be expected to be intermediate between parenchymal tissues and blood vessels. If this is the case, it is plausible that OPs can exit from bone tissue via the sinusoids, whose S1P concentration can only activate S1PR1 but not S1PR2. The concept that sinusoids are the place of OP mobilization agrees with our observation that sinusoidal cells have high motility in JTE-treated BM (Fig. S2).

This study clearly demonstrates that reciprocal actions of two S1P receptors regulate the steady-state migration propensities of OPs, constituting a versatile cycle that may play a crucial role in control of osteoclastogenesis and bone remodeling. Although therapeutics in bone-resorptive disorders have so far been targeted mature OCs (such as bisphosphonates) or late OPs fairly committed to OC differentiation (such as denosumab, i.e., anti-RANKL neutralizing antibody), treatment targeting monocytoid early OPs, such as S1P modulators, might be promising as a novel line of treatment in these disorders.

MATERIALS AND METHODS

Cell culture. RAW264.7, a mouse macrophage/monocyte lineage cell line, and mouse BM-derived M-CSF–dependent monocytes (BM-MDM), containing OP cells, were cultured as previously described (Ishii et al., 2006). To stimulate osteoclastogenesis, 50 ng/ml RANKL (PeproTech) was added to the medium and the cells were incubated for 3–4 d. In some experiments, cell were pretreated with siRNAs targeting S1PR1 or S1PR2 (ON-TARGET plus siRNA library; Thermo Fisher Scientific) using a conventional transfection reagent (Lipofectamine 2000; Invitrogen).

In vitro chemotaxis chamber assay. Chemotactic migration of cells was measured in a modified Boyden chamber as described previously (Okamoto et al., 2000).

EZ-Taxiscan chemotaxis assay. Chemotaxis experiments were also conducted in an EZ-Taxiscan chamber according to the manufacturer's protocol (Effector Cell Institute). The EZ-Taxiscan is a visually accessible chemotactic chamber, in which one compartment, containing ligand (S1P), and another compartment, containing cells, are connected by a microchannel. A stable concentration gradient of chemoattractant can be reproducibly formed and maintained through the channel without medium flow. Phase-contrast images of migrating cells were acquired at 1-min intervals. Sequential image data were processed with ImageJ (National Institutes of Health [NIH]), equipped with an add-on program, MT Track J.

Mice. C57BL/6 mice and CX_3CR1-EGFP knockin mice (Jung et al., 2000) were obtained from The Jackson Laboratory. *S1PR2*-defiicient mice (Kono et al., 2004) were obtained from R.L. Proia (National Institute of Diabetes and Digestive and Kidney Diseases, NIH, Bethesda, MD). All mice were bred and maintained under specific pathogen-free conditions at animal facilities of NIH and Osaka University, and all the animal experiments were performed according to NIH institutional guidelines and Osaka University animal experimental guidelines under approved protocols. Mutant mice were genotyped by PCR. All mice were housed and handled according to the institutional guidelines under approved protocols.

Two-photon intravital bone tissue imaging. Intravital microscopy of mouse calvaria bone tissues was performed using a protocol modified from a previous study (Ishii et al., 2009). Mice were anesthetized with isoflurane (Escain; 2.5% vaporized in an 80:20 mixture of O_2 and air), and the hair in the neck and scalp was removed with hair removal lotion (Epilat). The frontoparietal skull was exposed and the mouse head was immobilized in a custom-made stereotactic holder. A catheter was placed into the tail vein with a 30-gauge needle attached to PE-10 tubing (BD). The imaging system was composed of a multiphoton microscope (SP5; Leica) driven by a laser (MaiTai HP Ti:Sapphire; Spectraphysics) tuned to 880 nm and an upright microscope (DM6000B; Leica) equipped with a 20× water immersion objective (HCX APO, N.A. 1.0; Leica). The microscope was enclosed in an environmental chamber in which anesthetized mice were warmed by heated air. Fluorescent cells were detected through a bandpass emission filter at 525/50 nm (for EGFP). Vessels were visualized by injecting 70 kD of Texas red–conjugated dextran (detected using a 650/50 nm filter) i.v. immediately before imaging. In some experiments, 3 mg/kg JTE013 (Tocris Bioscience) dissolved in a vehicle (PBS containing 5% acidified DMSO and 3% fatty acid–free BSA) or vehicle only was injected during the imaging. Image stacks were collected at a 3-μm vertical step size at a depth of 100–150 μm below the skull bone surface. For 3D videos, four sequential image stacks were acquired at 3-μm z spacing to cover a volume of 154 μm × 154 μm × 9.0 μm. The time resolution was 1 min. Raw imaging data were processed with Imaris (Bitplane) with a Gaussian filter for noise reduction. Automatic 3D object tracking with Imaris Spots was aided with manual corrections to retrieve cell spatial coordinates over time.

Mouse treatment experiment. Nine 8-wk-old female, wild-type, or $S1PR2^{-/-}$ mice were injected i.p. with PBS, 2 mg/kg GST-RANKL dissolved in PBS (Tomimori et al., 2009), and 2 mg/kg GST-RANKL and 3 mg/kg JTE013 (dissolved in PBS containing 5% acidified DMSO and 3% fatty acid–free BSA) for 2 d. The mice were then sacrificed and femurs were excised and subjected to histomorphometrical analyses.

Histomorphometry of bone tissues. Trabecular bone morphometry within the metaphyseal region of distal femur was quantified using micro-CT

Published December 6, 2010

(ScanXmate-RX; Comscantechno Inc.). 3D microstructural image data were reconstructed, and structural indices, such as B.V./T.V., Tb.Th., and Tb.N., were calculated using TRI/3D-BON software (RATOC Systems). Bone morphometric analysis was performed as previously described (Parfitt et al., 1987).

Flow cytometry. All reagents were purchased from BD. To examine the composition of peripheral blood mononuclear cells, blood was collected from the retroorbital plexus with a heparinized glass pipette from mice treated i.p. 2 h previously with 3 mg/kg JTE013 or vehicle. After removing the red blood cells by ACK lysis buffer (Invitrogen), cells were stained with FITC-conjugated anti-CD11b and PE-Cy7–conjugated anti-CD3, using conventional methods. Flow cytometric data were collected on a FACSCanto II (BD) and analyzed with FlowJo software (Tree Star, Inc.).

Statistics. The Mann-Whitney rank sum test was used to calculate p-values for highly skewed distributions. For Gaussian-like distributions, two-tailed Student's *t* tests were used.

Online supplemental material. Fig. S1 shows chemotaxis and in vitro osteoclastogenesis of S1PR2 knockout OPs. Fig. S2 shows in vivo S1PR2-mediated migration control of CX_3CR1^+ OP monocytes visualized using intravital two-photon imaging. Fig. S3 shows the therapeutic effect of S1PR2 antagonist JTE013 on ovariectomy-induced osteoporosis and schematic model for S1P-mediated localization control of OPs in bone tissues. Videos 1–6 show in vitro chemotaxis of RAW264.7 cells toward an S1P gradient detected using the EZ-Taxiscan device. Videos 7 and 8 show intravital two-photon imaging of mouse skull bone tissues of CX_3CR1-EGFP hetero knockin mice. Video 9 shows intravital two-photon imaging (broad visual field) of mouse skull bone tissues of CX_3CR1-EGFP heterozygous knockin mice. Online supplemental material is available at http://www.jem.org/cgi/content/full/jem.20101474/DC1.

We thank Dr. Richard L. Proia (National Institute of Diabetes and Digestive and Kidney Diseases, National Institutes of Health [NIH]) for S1PR2-deficient mice.

This work was supported in part by the Intramural Research Program of the National Institute of Allergy and Infectious Diseases, NIH, United States Department of Health and Human Services (R.N. Germain), by grants from the International Human Frontier Science Program (LT-00387/2006-L and CDA-00059/2009; to M. Ishii), by a Grants-in-Aid for Encouragement of Young Scientists (A; 22689030), for Scientific Research on Innovative Areas (22113007; to M. Ishii), and a Funding Program for World-Leading Innovative R&D on Science and Technology (FIRST Program) from the Ministry of Education, Science, Sports and Culture of Japan, by Grants-in-Aid for Research on Allergic Disease and Immunology (H21-010; to M. Ishii) from the Ministry of Health, Labor and Welfare of Japan, and by Grants from Takeda Science Foundation (to M. Ishii), from Japan Research Foundation for Clinical Pharmacology (to M. Ishii), from Senri Lifescience Foundation (to M. Ishii), and from Mochida Memorial Foundation for Medical and Pharmaceutical Research (to M. Ishii).

The authors declare no competing financial interests.

Submitted: 22 July 2010
Accepted: 10 November 2010

REFERENCES

Binder, N.B., B. Niederreiter, O. Hoffmann, R. Stange, T. Pap, T.M. Stulnig, M. Mack, R.G. Erben, J.S. Smolen, and K. Redlich. 2009. Estrogen-dependent and C-C chemokine receptor-2-dependent pathways determine osteoclast behavior in osteoporosis. *Nat. Med.* 15:417–424. doi:10.1038/nm.1945

Gronthos, S., and A.C. Zannettino. 2007. The role of the chemokine CXCL12 in osteoclastogenesis. *Trends Endocrinol. Metab.* 18:108–113. doi:10.1016/j.tem.2007.02.002

Ishii, M., K. Iwai, M. Koike, S. Ohshima, E. Kudo-Tanaka, T. Ishii, T. Mima, Y. Katada, K. Miyatake, Y. Uchiyama, and Y. Saeki. 2006. RANKL-induced expression of tetraspanin CD9 in lipid raft membrane microdomain is essential for cell fusion during osteoclastogenesis. *J. Bone Miner. Res.* 21:965–976. doi:10.1359/jbmr.060308

Ishii, M., J.G. Egen, F. Klauschen, M. Meier-Schellersheim, Y. Saeki, J. Vacher, R.L. Proia, and R.N. Germain. 2009. Sphingosine-1-phosphate mobilizes osteoclast precursors and regulates bone homeostasis. *Nature.* 458:524–528. doi:10.1038/nature07713

Jung, S., J. Aliberti, P. Graemmel, M.J. Sunshine, G.W. Kreutzberg, A. Sher, and D.R. Littman. 2000. Analysis of fractalkine receptor CX_3CR1 function by targeted deletion and green fluorescent protein reporter gene insertion. *Mol. Cell. Biol.* 20:4106–4114. doi:10.1128/MCB.20.11.4106-4114.2000

Karsenty, G., and E.F. Wagner. 2002. Reaching a genetic and molecular understanding of skeletal development. *Dev. Cell.* 2:389–406. doi:10.1016/S1534-5807(02)00157-0

Klauschen, F., M. Ishii, H. Qi, M. Bajénoff, J.G. Egen, R.N. Germain, and M. Meier-Schellersheim. 2009. Quantifying cellular interaction dynamics in 3D fluorescence microscopy data. *Nat. Protoc.* 4:1305–1311. doi:10.1038/nprot.2009.129

Kono, M., Y. Mi, Y. Liu, T. Sasaki, M.L. Allende, Y.P. Wu, T. Yamashita, and R.L. Proia. 2004. The sphingosine-1-phosphate receptors S1P1, S1P2, and S1P3 function coordinately during embryonic angiogenesis. *J. Biol. Chem.* 279:29367–29373. doi:10.1074/jbc.M403937200

Maeda, Y., N. Seki, N. Sato, K. Sugahara, and K. Chiba. 2010. Sphingosine 1-phosphate receptor type 1 regulates egress of mature T cells from mouse bone marrow. *Int. Immunol.* 22:515–525. doi:10.1093/intimm/dxq036

Mazo, I.B., M. Honczarenko, H. Leung, L.L. Cavanagh, R. Bonasio, W. Weninger, K. Engelke, L. Xia, R.P. McEver, P.A. Koni, et al. 2005. Bone marrow is a major reservoir and site of recruitment for central memory $CD8^+$ T cells. *Immunity.* 22:259–270. doi:10.1016/j.immuni.2005.01.008

Niess, J.H., S. Brand, X. Gu, L. Landsman, S. Jung, B.A. McCormick, J.M. Vyas, M. Boes, H.L. Ploegh, J.G. Fox, et al. 2005. CX_3CR1-mediated dendritic cell access to the intestinal lumen and bacterial clearance. *Science.* 307:254–258. doi:10.1126/science.1102901

Okamoto, H., N. Takuwa, T. Yokomizo, N. Sugimoto, S. Sakurada, H. Shigematsu, and Y. Takuwa. 2000. Inhibitory regulation of Rac activation, membrane ruffling, and cell migration by the G protein-coupled sphingosine-1-phosphate receptor EDG5 but not EDG1 or EDG3. *Mol. Cell. Biol.* 20:9247–9261. doi:10.1128/MCB.20.24.9247-9261.2000

Onan, D., E.H. Allan, J.M. Quinn, J.H. Gooi, S. Pompolo, N.A. Sims, M.T. Gillespie, and T.J. Martin. 2009. The chemokine Cxcl1 is a novel target gene of parathyroid hormone (PTH)/PTH-related protein in committed osteoblasts. *Endocrinology.* 150:2244–2253. doi:10.1210/en.2008-1597

Osada, M., Y. Yatomi, T. Ohmori, H. Ikeda, and Y. Ozaki. 2002. Enhancement of sphingosine 1-phosphate-induced migration of vascular endothelial cells and smooth muscle cells by an EDG-5 antagonist. *Biochem. Biophys. Res. Commun.* 299:483–487. doi:10.1016/S0006-291X(02)02671-2

Parfitt, A.M., M.K. Drezner, F.H. Glorieux, J.A. Kanis, H. Malluche, P.J. Meunier, S.M. Ott, and R.R. Recker; Report of the ASBMR Histomorphometry Nomenclature Committee. 1987. Bone histomorphometry: standardization of nomenclature, symbols, and units. *J. Bone Miner. Res.* 2:595–610. doi:10.1002/jbmr.5650020617

Rosen, H., and E.J. Goetzl. 2005. Sphingosine 1-phosphate and its receptors: an autocrine and paracrine network. *Nat. Rev. Immunol.* 5:560–570. doi:10.1038/nri1650

Takuwa, Y. 2002. Subtype-specific differential regulation of Rho family G proteins and cell migration by the Edg family sphingosine-1-phosphate receptors. *Biochim. Biophys. Acta.* 1582:112–120.

Teitelbaum, S.L. 2000. Bone resorption by osteoclasts. *Science.* 289:1504–1508. doi:10.1126/science.289.5484.1504

Teitelbaum, S.L., and F.P. Ross. 2003. Genetic regulation of osteoclast development and function. *Nat. Rev. Genet.* 4:638–649. doi:10.1038/nrg1122

Tomimori, Y., K. Mori, M. Koide, Y. Nakamichi, T. Ninomiya, N. Udagawa, and H. Yasuda. 2009. Evaluation of pharmaceuticals with a novel 50-hour animal model of bone loss. *J. Bone Miner. Res.* 24:1194–1205. doi:10.1359/jbmr.090217

Yang, M., G. Mailhot, C.A. MacKay, A. Mason-Savas, J. Aubin, and P.R. Odgren. 2006. Chemokine and chemokine receptor expression during colony stimulating factor-1-induced osteoclast differentiation in the toothless osteopetrotic rat: a key role for CCL9 (MIP-1γ) in osteoclastogenesis in vivo and in vitro. *Blood.* 107:2262–2270. doi:10.1182/blood-2005-08-3365

PHILOSOPHICAL TRANSACTIONS OF THE ROYAL SOCIETY A

Phil. Trans. R. Soc. A (2010) **368**, 2983–3000
doi:10.1098/rsta.2010.0093

Cellular modelling: experiments and simulation to develop a physiological model of G-protein control of muscarinic K^+ channels in mammalian atrial cells

By Shingo Murakami[1,2,*], Shingo Suzuki[1,3], Masaru Ishii[1,4], Atsushi Inanobe[1,2] and Yoshihisa Kurachi[1,2,*]

[1]*Division of Molecular and Cellular Pharmacology, Department of Pharmacology, Graduate School of Medicine, and* [2]*The Center for Advanced Medical Engineering and Informatics, Osaka University, 2-2 Yamada-oka, Suita, Osaka 565-0871, Japan*
[3]*Graduate School of Engineering Science, Osaka University, 1-3 Machikaneyama-cho, Toyonaka, Osaka 560-0043, Japan*
[4]*Laboratory of Biological Imaging, WPI-Immunology Frontier Research Center, Osaka University, 3-1 Yamada-oka, Suita, Osaka 565-0871, Japan*

The first model of G-protein–K_{ACh} channel interaction was developed 14 years ago and then expanded to include both the receptor–G-protein cycle and G-protein–K_{ACh} channel interaction. The G-protein–K_{ACh} channel interaction used the Monod–Wyman–Changeux allosteric model with the idea that one K_{ACh} channel is composed of four subunits, each of which binds one active G-protein subunit ($G_{\beta\gamma}$). The receptor–G-protein cycle used a previous model to account for the steady-state relationship between K_{ACh} current and intracellular guanosine-5-triphosphate at various extracellular concentrations of acetylcholine (ACh). However, simulations of the activation and deactivation of K_{ACh} current upon ACh application or removal were much slower than experimental results. This clearly indicates some essential elements were absent from the model. We recently found that regulators of G-protein signalling are involved in the control of K_{ACh} channel activity. They are responsible for the voltage-dependent relaxation behaviour of K_{ACh} channels. Based on this finding, we have improved the receptor–G-protein cycle model to reproduce the relaxation behaviour. With this modification, the activation and deactivation of K_{ACh} current in the model are much faster and now fall within physiological ranges.

Keywords: G-protein; GIRK channel; relaxation; heart; atria; computational model

*Authors for correspondence (murakami@pharma2.med.osaka-u.ac.jp; ykurachi@pharma2.med.osaka-u.ac.jp).

One contribution of 13 to a Theme Issue 'The virtual physiological human: computer simulation for integrative biomedicine II'.

1. Introduction

G-protein-coupled receptors (GPCR) make up a large part of the human genome, and they and the G-protein intracellular signalling pathways are involved in the regulation of the cardiovascular system. Defects in the expression and regulation of GPCRs and/or G-proteins underlie various cardiovascular defects and diseases (Smith & Luttrell 2006; Alemany *et al.* 2007), contributing to heart failure (Meij 1996; Feldman *et al.* 2008) and cardiac hypertrophy (Akhter *et al.* 1998; Sakata *et al.* 1998; Barry *et al.* 2008). The G-protein signalling pathways are therefore regarded as therapy targets for cardiovascular diseases and their characteristics need to be understood quantitatively (Alemany *et al.* 2007). Mathematical models of G-protein signalling can play an important role in developing quantitative understanding of these signalling pathways (Thomsen *et al.* 1988; Mackay 1990; Felber *et al.* 1996; Mosser *et al.* 2002; Hao *et al.* 2003; Saucerman *et al.* 2003; Yi *et al.* 2003; Zhong *et al.* 2003; Suh *et al.* 2004; Katanaev & Chornomorets 2007; Linderman 2009). In the heart, models of sympathetic control of voltage-dependent inactivation in the L-type Ca^{2+} channel (Faber & Rudy 2007; Findlay *et al.* 2008) and a biochemical pathway model for β-adrenergic receptor stimulation (Saucerman *et al.* 2003) have been developed. Models of β-adrenergic signalling in the rat ventricular myocyte (Saucerman *et al.* 2003) and modulation of the M-current based upon KCNQ2/KCNQ3 channel subunits expressed in a cell line (Suh *et al.* 2004) were formulated from biochemical assays. To date there have been few models of parasympathetic control (Hosoya *et al.* 1996; Demir *et al.* 1999; Hosoya & Kurachi 1999). In this article, we present the most recent developments of our model of acetylcholine (ACh) activation of cardiac muscarinic K^+ (K_{ACh}) channels. The activation of the K_{ACh} channel is mediated by the βγ subunit ($G_{\beta\gamma}$) of PTX-sensitive G-proteins (G_K) coupled to m_2 or A_1 purinergic receptors in the cardiac cell membrane (Kurachi *et al.* 1986, 1989; Logothetis *et al.* 1987, 1988). Thus, the model is a composite involving the receptor–G-protein cycle and the interaction between the G-protein and K_{ACh} channel.

K_{ACh} channels are activated by intracellular guanosine-5′-triphosphate (GTP_i) in a highly positive cooperative manner at any given concentration of extracellular ACh ($[ACh]_0$) and as the concentration of ACh is increased, both the apparent potency and efficacy of GTP_i are also increased (figure 1*a*,*b*; Kurachi *et al.* 1990; Ito *et al.* 1991). This may reflect properties of the G_K protein–K_{ACh} channel interaction which can be accounted for by the Monod–Wyman–Changeux (MWC) allosteric model with the idea that one K_{ACh} channel is composed of at least four functionally identical subunits, each of which binds one $G_{K\beta\gamma}$ (figure 1*c*; Hosoya *et al.* 1996). For the receptor–G-protein cycle we adopted the model of a receptor-mediated trimeric G-protein reaction cycle developed by Thomsen *et al.* (1988) (figure 1*d*(i)). We combined the two models to construct an integrated model of ACh activation of K_{ACh} channels (Hosoya & Kurachi 1999) which reproduced the steady-state relationship between K_{ACh} channel activity and GTP_i at various $[ACh]_0$ (figure 1*b*).

In isolated atrial myocytes, ACh (0.1 μM) evokes the K_{ACh} current with a half time for activation of 500 ms (Ishii *et al.* 2001). Upon removal of ACh (1.1 μM) from the bath, the current deactivates with a half time of 3.7 s (figure 1*e*; Kurachi *et al.* 1987). The integrated model (Hosoya & Kurachi 1999) could not accurately

reproduce this temporal behaviour of the K_{ACh} current, rather the half time for activation was approximately 1 min and that for deactivation was approximately 2.5 min (figure 1*f*(i, ii); Kurachi & Ishii 2004). Clearly, the model was incomplete.

The K_{ACh} current exhibits strong inward rectification which is caused by Mg^{2+} and polyamines blocking outwardly flowing current. Upon hyperpolarization from a holding potential of -40 mV, the current increases in two distinct phases: instantaneous and slow time-dependent phases. The initial instantaneous increase is due to unblocking of Mg^{2+} and polyamines. The following gradual current increase, which is called 'relaxation', reflects a slow recovery from the reduction of the product of K_{ACh} channel number and K_{ACh} channel open probability (NP_o) that occurs at depolarized potentials. Recently, we have found that regulators of G-protein signalling (RGSs) are involved in this phenomenon (Ishii *et al.* 2001, 2002). RGS proteins stimulate the GTPase activity of the α subunit of G_K proteins ($G_{K\alpha}$) and decrease G_K protein activation (Hepler 1999; Ross & Wilkie 2000). In the resting state this action of an RGS protein is inhibited by the binding of $PtdIns(3,4,5)P_3$. A Ca^{2+}/calmodulin (CaM) complex, which is formed following depolarization-induced Ca^{2+}-influx across the cardiac cell membrane, displaces $PtdIns(3,4,5)P_3$ and relieves the inhibition. The activated RGS proteins decrease the activated G_K proteins and thus K_{ACh} channel activity at depolarized potentials. This series of experimental results strongly suggest that relaxation directly reflects G_K protein activity coupling to the K_{ACh} channel. Thus, by analysing the relaxation behaviour of the K_{ACh} current, the physiological kinetics of the receptor-mediated G_K reaction cycle can be obtained. Here we incorporate these ideas into the model of ACh activation of the K_{ACh} channel and we present the model in this paper.

2. Material and methods

(*a*) *Modelling*

The model consists of two parts: an allosteric model representing the interaction between $G_{K\beta\gamma}$ and K_{ACh} channels, and a G-protein cycle model representing the interaction between muscarinic receptors and G_K proteins (figure 1*c*,*d*(ii)). The parameters were searched and verified by comparing the model and experimental results (see §3 and appendix A for details).

(*b*) *Electrophysiological measurements*

Experiments were performed in accordance with the guidelines for the use of laboratory animals of Osaka University. The experimental protocol used here is explained in Ishii *et al.* (2002). In brief, single atrial myocytes were enzymatically isolated from hearts removed from adult male Wister-Kyoto rats. The K_{ACh} currents evoked by various concentrations of ACh were recorded in the whole-cell configuration of the patch-clamp technique. Other experimental data, such as single channel current recording, were taken from published papers (Kurachi *et al.* 1986; Ito *et al.* 1991).

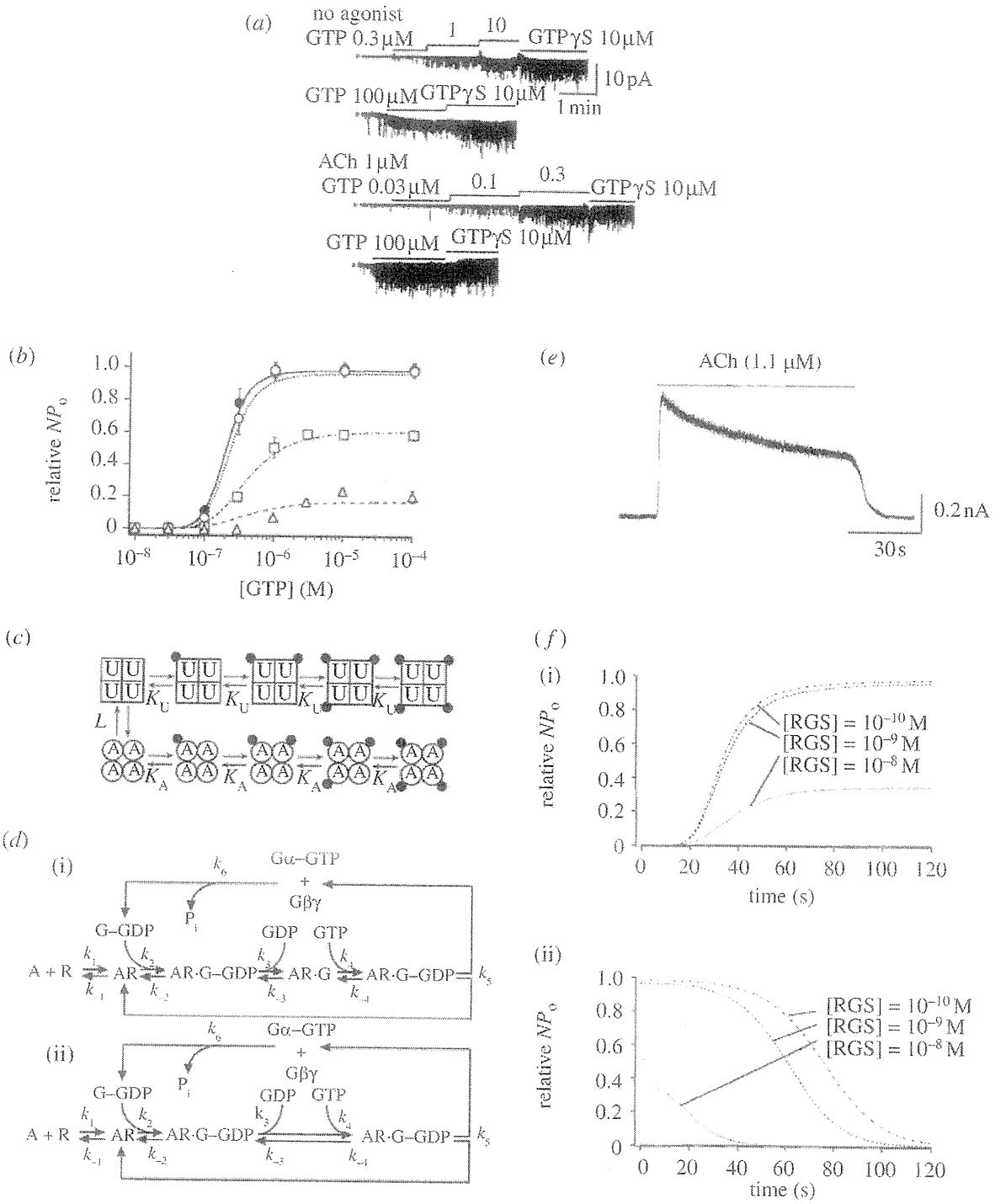

Figure 1. (*Caption opposite.*)

3. Results

(a) *The MWC allosteric model applied to G_K protein–K_{ACh} channel interaction*

Cardiac K_{ACh} channels are activated directly by $G_{\beta\gamma}$ proteins (Logothetis *et al.* 1987, 1988; Kurachi *et al.* 1989). Here, we used the MWC allosteric model (Monod *et al.* 1965) to simulate the interaction between $G_{\beta\gamma}$ and K_{ACh} channels

Figure 1. (*Opposite.*) Previous experimental and simulation studies on K_{ACh} channels. (*a*) Examples of inside-out patch experiments obtained from guinea pig atrial myocytes. The concentration of acetylcholine ([ACh]) in the pipette was 0 or 1 μM as indicated. The bars above each trace indicate the periods of application of the various concentrations of GTP and 10 μM GTPγS to the internal side of the patch membrane. The holding potential was −80 mV. Note that a 3- to 10-fold increase in GTP concentration resulted in a dramatic increase in channel open probability (NP_o) of K_{ACh} channels, indicating the existence of a highly positive cooperative process. (*b*) The experimental relationship between the concentration of GTP and the NP_o of K_{ACh} channels normalized to the maximum NP_o induced by 10 μM GTPγS in each patch (symbols and bars are mean ± s.d.), shown with simulated results obtained with the previous integrated model (Hosoya & Kurachi 1999) of the Monod–Wyman–Changeux (MWC) allosteric model and the Thomsen–Jaquez–Neubig model (lines). [ACh] = 10^{-6} M (filled circles), 10^{-7} M (open circles), 10^{-8} M (squares), 0 M (triangles). (*c*) Schematic of the MWC allosteric model. In this scheme, each K_{ACh} channel is assumed to be an oligomer composed of four identical subunits (i.e. $n = 4$). Each subunit is in either the available (A) or the unavailable (U) state, represented by circles and squares, respectively. Each subunit in the A or U state binds with one dissociated G-protein βγ subunit (filled circles) independently of other subunits, with microscopic dissociation constants K_A or K_U, respectively. In this model, all subunits in the same oligomer must change their conformations simultaneously. Therefore, the channel can be either A_4 or U_4. A_4 and U_4 are in equilibrium through an allosteric constant L. (*d*) Models for receptor–G-protein interaction. (i) Thomsen–Jaquez–Neubig model for receptor–G-protein interaction in the previous model (Hosoya & Kurachi 1999). A, acetylcholine; R, muscarinic m_2-receptor; G, G-protein. (ii) The modified model for receptor–G-protein interaction used in the present study. AR·G is removed and k_6 parameter has been modified. (*e*) The experimental time courses of activation and deactivation phases of 1.1 μM ACh-induced K_G channel currents. (*f*) The simulated time courses of (i) activation and (ii) deactivation phases of 1 μM ACh-induced K_G channel currents in the presence of various concentrations of RGS. The RGS protein action was assumed to be voltage-independent in this prior simulation study (Kurachi & Ishii 2004). RGS accelerated the time course of deactivation but did not affect the activation time course. RGS at high concentrations suppressed maximal channel activity (*a*,*b*). Reproduced and modified from (*a*) Ito *et al.* (1991), (*b*) Hosoya & Kurachi (1999), (*e*) Kurachi *et al.* (1987) and (*f*) Kurachi & Ishii (2004).

in similar ways to Hosoya *et al.* (1996) and Hosoya & Kurachi (1999). In the present study we re-fitted the three parameters of the MWC model to improve the accuracy of the allosteric model. Corey & Clapham (2001) assayed biochemically the profile of $G_{\beta\gamma}$ subunit binding to K_{ACh} channels (GIRK4). They showed that from one to four $G_{\beta\gamma}$ subunits actually bind to one K_{ACh} channel (figure 2*a*, exp.). By comparing the $G_{\beta\gamma}$-binding profile in the actual assay and that estimated by the MWC model, we examined the validity of the parameters that had been used in the previous studies (Hosoya *et al.* 1996; Hosoya & Kurachi 1999; figure 2*a*). The concentration-dependent activation of the K_{ACh} channel by $G_{\beta\gamma}$ and GTP in inside-out patches can be reproduced only with allosteric models (Hosoya *et al.* 1996) and since we now know that a K_{ACh} channel is a tetramer of Kir3.x protein subunits (Corey & Clapham 2001) an allosteric mechanism most probably underlies the activation process. In the MWC model a K_{ACh} channel consists of four protein units (Kir3.x; figure 1*c*). All of the Kir units in a given channel are defined as being in the same state, either tense (T) or relaxed (R), and change their state together (concerted transition). One $G_{\beta\gamma}$

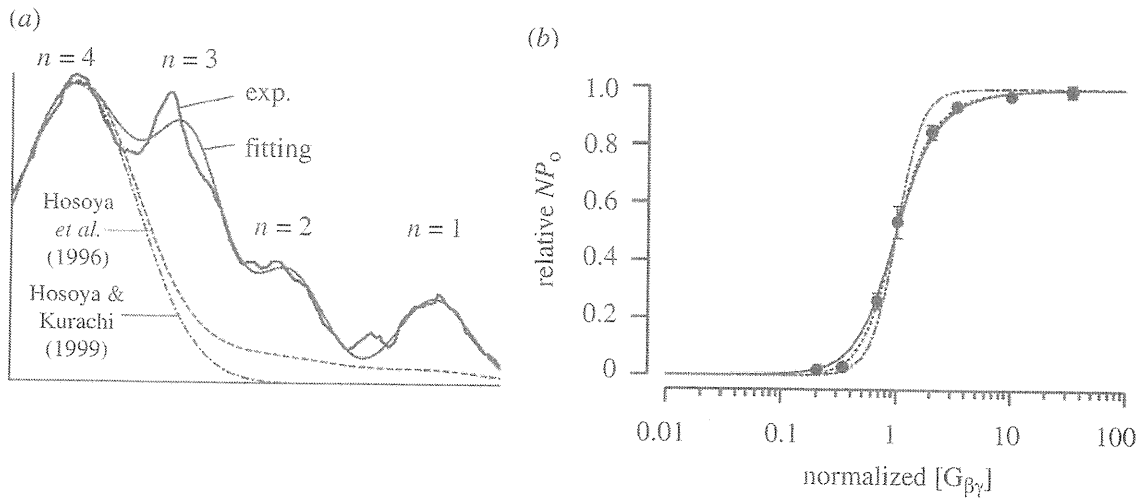

Figure 2. $G_{\beta\gamma}$ protein binding to GIRK channels. (*a*) The densitometry profile of membranes containing GIRK4 with $G_{\beta\gamma}$. Experimental data (exp.) was obtained by densitometry from fig. 3*d* of Corey & Clapham (2001; *n*, the estimated number of $G_{\beta\gamma}$ proteins per channel). Lines represent the densitometry profiles calculated with the parameter sets from the present study (fitting), Hosoya *et al.* (1996) and Hosoya & Kurachi (1999). (*b*) The concentration–response relationship between $G_{\beta\gamma}$ proteins and K_{ACh} channel opening. The fractions of K_{ACh} channels in the open state were calculated with the parameter sets from the present study (solid line), Hosoya *et al.* (1996) (dotted line), and Hosoya & Kurachi (1999) (dot-dash line). Experimental data (circles) from Hosoya *et al.* (1996) were normalized for $G_{\beta\gamma}$ concentration.

protein equilibrates with one Kir protein in either tense or relaxed states with separate equilibrium constants defined as K_T for tense and K_R for relaxed. A tetramer without any $G_{\beta\gamma}$ equilibrates between tense and relaxed states according to the equilibrium constant L. Channels in the relaxed state are considered as available to open with fast gating kinetics (equation (A 1) in appendix A, NP_o), and channels in the tense state are considered to be unavailable (see Hosoya *et al.* 1996 for details).

In the previous studies simulation with the MWC model for G_K–K_{ACh} channel interaction assumed that the majority of the K_{ACh} channels would bind with four $G_{K\beta\gamma}$ subunits, and the numbers of channels binding one, two, or three $G_{K\beta\gamma}$ subunits were practically negligible (figure 2*a*; Hosoya *et al.* 1996; Hosoya & Kurachi 1999). However, the biochemical assay showed that K_{ACh} channels binding one, two, three and four $G_{\beta\gamma}$ represent, respectively, approximately 10, 10, 40 and 40 per cent of the total channel population (figure 2*a*, exp.). Therefore, the parameters used for the MWC model in the previous studies were clearly invalid. In the present study, therefore, the parameters K_T, K_R and L (table 1) were re-calculated with the simplex method to reproduce the densitometry profiles of membranes containing GIRK4 preincubated with $G_{\beta\gamma}$. With the new parameters, the MWC model for the $G_{K\beta\gamma}$–K_{ACh} channel interaction well reproduced the biochemical experimental results (figure 2*a*, fitting).

Figure 2*b* shows the relationships between the K_{ACh} channel NP_o and $[G_{K\beta\gamma}]$ calculated by using the MWC model with the parameter sets used in the previous studies and the present study. The $[G_{K\beta\gamma}]$ values were normalized at the half maximum of the K_{ACh} channel activity. Although L values in the three sets were quite different, all of the relationships exhibited the positive cooperative effect of

Table 1. Parameters of the allosteric and G-protein cycle models.

parameter	value	unit
L	1405	dimensionless
K_R	5.00×10^{-8}	M
K_T	9.09×10^{-7}	M
K_R/K_T	0.0550	dimensionless
k_1	1.67×10^{6}	$s^{-1}\ M^{-1}$
k_{-1}	0.167	s^{-1}
k_2[G–GDP]	1.80×10^{-2} [G–GDP]	s^{-1}
k_{-2}	0.1	s^{-1}
$k_{3,4}$	2.86×10^{3}	$s^{-1}\ M^{-1}$
$k_{-4,-3}$[GDP]	6.8×10^{-4}	s^{-1}
k_5	10	s^{-1}
k_6	$1.13\left(1 + \frac{1.30}{1 + \exp(-0.042(V + 25))}\right)$	s^{-1}
$[R]_{total}$	1.87×10^{-3}	M
$[G]_{total}/[R]_{total=}$	30	dimensionless

$[G_{K\beta\gamma}]$ on the K_{ACh} channel NP_o, and the relationship obtained by using the new parameters agrees well with the experimental data. We therefore used the new set of parameters for the MWC model in the following studies.

(*b*) *The G-protein cycle model*

The other part of the ACh activation of cardiac K_{ACh} channel model is the G_K protein cycle which produces $G_{K\beta\gamma}$ subunits. At first, we tested two G-protein cycle models: the Thomsen–Jaquez–Neubig model (Thomsen *et al.* 1988; figure 1*d*(i)) and the Mackay model (Mackay 1990) to see if they could reproduce various characteristics of ACh activation of the K_{ACh} channel. However, after considerable trial and error, we found that neither model was satisfactory when we tried to reproduce at various $[ACh]_0$ not only the steady-state relationship between GTP_i and K_{ACh} channel activity, but also the relationship between the membrane potential and the steady state NP_o of K_{ACh} channels and the voltage-dependent relaxation behaviour. In the present study, we modified the Thomsen–Jaquez–Neubig model. This modified G_K-protein cycle model (figure 1*d*(ii)) is a model of chemical reaction kinetics consisting of concentrations and reaction rate constants (k). AR·G was removed and the k_6 parameter was modified from the original Thomsen–Jaquez–Neubig model. Six values of concentration ([R], [AR], [ARG–GDP], [ARG–GTP], [G–GTP] and [G–GDP] for ACh (A), m_2-receptor (R), G_K protein (G)) in the G-protein cycle model are updated at each calculation step with six ordinary differential equations (equations (A 2)–(A 7) in appendix A). In the previous studies all of the values of rate constants were fixed (figure 1*d*(i)). A novel aspect of the modified model (figure 1*d*(ii)) in the present study is that we have incorporated the concept of regulation of G-protein signalling (RGS). RGS proteins regulate G-protein signalling by accelerating GTP

hydrolysis, and they may be involved in the development of certain cardiovascular pathologies (Wieland & Mittmann 2003; Semplicini *et al.* 2006; Wieland *et al.* 2007; Hendriks-Balk *et al.* 2008). Modulation of GTP hydrolysis by RGS proteins also underlies a voltage- and time-dependent character of the K_{ACh} current in atrial myocytes known as 'relaxation' (figure 3*b*; Inanobe *et al.* 2001; Ishii *et al.* 2001, 2002). Relaxation of the K_{ACh} current reflects an increasing suppression of channel open probability during depolarization and a gradual recovery during hyperpolarization. The time course of these phenomena depends upon voltage-dependent Ca^{2+} influx and Ca^{2+}/CaM modulation of RGS protein activity (Ishii *et al.* 2001). Therefore, GTPase activity of $G_{K\alpha}$ in atrial myocytes can be modulated by RGS proteins in a voltage-dependent manner (Ishii *et al.* 2001). In the modified G_K-cycle model used in the present study, the action of RGS proteins is expressed by the new parameter k_6. The value of each rate constant was fixed, except for k_6 (table 1). Parameter k_6 is defined as a function of membrane voltage so that depolarization of the membrane potential can accelerate GTPase activity (equation (A 8) in appendix A). The rate constants, the total concentration of the receptor ($[R]_{total}$) and a conversion multiplier between inside-out and whole cell recording (r; see §3*a*) were obtained by the simplex method searching for the best fit of the following three properties at various $[ACh]_0$: (i) the steady-state relationships between K_{ACh} channel open probability (NP_o) and GTP_i, (ii) the voltage dependence of K_{ACh} channel NP_o, and (iii) the relaxation time constants at various membrane potentials. We set the value of GTP_i to 100 μM in the whole cell current simulation because this concentration was used in the internal pipette solution in whole cell recording. The $[G_{K\beta\gamma}]$ generated by the G_K protein cycle model was taken into the allosteric model and then the K_{ACh} channel NP_o was calculated by using equation (A 1).

(*c*) *Analysis of simulations with the integrated model*

The improved MWC allosteric model for $G_{K\beta\gamma}$–K_{ACh} channel interaction and the modified G_K protein cycle model were combined into a new integrated model for ACh activation of K_{ACh} channels. The properties of the K_{ACh} current in the integrated model were examined as follows.

(i) *The steady-state relationship between K_{ACh} channel activity and GTP_i*

Since intracellular GTP was not changed in whole cell recording, experimental inside-out patch data for the effect of [GTP] in the presence of different $[ACh]_0$ were taken from Ito *et al.* (1991), converted to that representing whole cell recording and shown as symbols in figure 3*a*. Both GTP and ACh increased K_{ACh} channel activity in a concentration-dependent manner. GTP_i activated the K_{ACh} channel in excised membrane patches much more potently than in whole cell recording. This is probably because in the inside-out patch experiments the internal solution contained high chloride which interferes with the GTPase activity of G_α and increases the sensitivity to GTP by shifting the GTP-relative NP_o curve by 100-fold (Nakajima *et al.* 1992, fig. 4). Therefore, we multiplied the concentration of GTP in excised membrane patch data by 100 to reproduce the GTP_i-dependence of whole cell K_{ACh} currents. Also in the inside-out patch experiments with the high chloride internal solution, GTP_i induced significant K_{ACh} channel activity in the absence of external ACh (figure 3*a*,

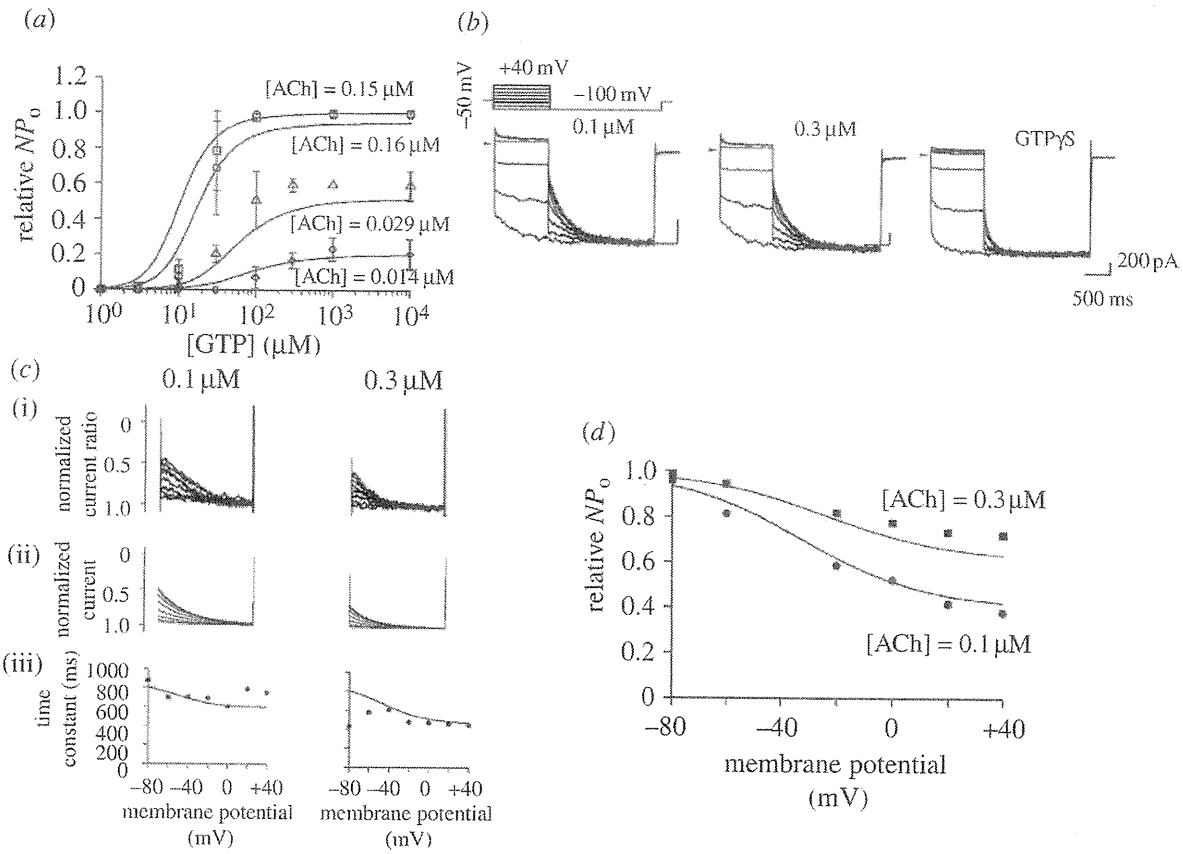

Figure 3. Voltage-dependent relaxation of K_{ACh} current. (*a*) The relationship between K_{ACh} channel open probability (NP_o) and GTP concentration in the presence of different concentrations of ACh. Symbols represent data from Ito *et al.* (1991) and lines represent data obtained from the new model. See text for further details. (*b*) Voltage-clamp single cell current recordings of voltage-dependent relaxation. Single rat atrial cells were subjected to the voltage-clamp protocol inset. Experiments were conducted in the presence of two different concentrations of ACh_0 and 3 μM intracellular GTPγS. (*c*) (i) Normalized K_{ACh} current relaxation traces for 0.1 and 0.3 μM ACh. (ii) Equivalent currents simulated by the model. (iii) Time constants of K_{ACh} current relaxation. Symbols represent experimental data and lines represent the results from model simulation. (*d*) The relationship between the relative K_{ACh} channel availability (NP_o) and prepulse voltage. Experimental data (dots) and simulated results (lines) are shown for ACh concentrations of 0.1 and 0.3 μM.

open diamonds; Nakajima *et al.* 1992, fig. 7). In whole cell recordings there was no detectable K_{ACh} current in the absence of ACh, since in the absence of ACh the G-protein cycle should not be activated at all. Since the basal K_{ACh} current, presumably due to the high chloride, is difficult to separate from the inside-out experimental data, only in this calculation we instead increased the [ACh] in experimental data by an equivalent of 0.01 μM to reproduce the experimental response to GTP in the absence of ACh (figure 3*a*, open diamonds) and then multiplied [ACh] by a fitted parameter of a multiplier r (1.44) to represent a lower sensitivity to ACh in whole cell recording. With these conversions, the model quantitatively reproduced the experimental data for the relationships between K_{ACh} channel activity and GTP_i at various $[ACh]_0$ (figure 3*a*, lines).

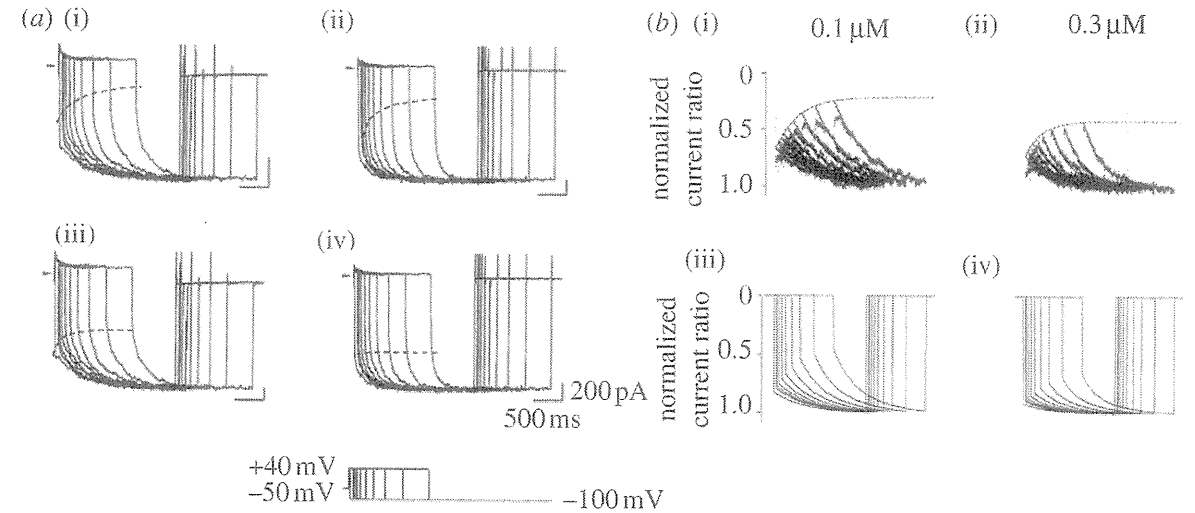

Figure 4. Time-dependent development of K_{ACh} current relaxation. (*a*) Voltage-clamp single cell current recordings from rat atrial cells obtained during a voltage step to −100 mV following a prepulse voltage step to +40 mV of variable duration (22–1306 ms) in cells exposed to either three different concentrations of ACh_0 or 3 μM intracellular GTPγS ((i) 0.1 μM, (ii) 0.3 μM, (iii) 3 μM, (iv) GTPγS). (*b*) (i,ii) Superimposed traces of relaxation currents recorded in the presence of two concentrations of ACh following prepulses of different durations. These currents have been normalized to data recorded in the presence of intracellular GTPγS. (iii,iv) Equivalent currents generated by the model.

(ii) *Voltage and time dependence of the K_{ACh} current*

Voltage- and time-dependent characteristics of the K_{ACh} current are revealed by the phenomenon of relaxation. The experimental relaxation behaviour of K_{ACh} current at various $[ACh]_0$ is shown in figure 3*b*. The preconditioning voltage steps from −100 mV to +40 mV (in 10 mV increments) were applied for 1 s and followed by a test voltage step (2 s in duration) to −100 mV. During the test voltage step relaxation is the slow increase in K_{ACh} current which is observed following a prior instantaneous depolarization (figure 3*b*). This represents the recovery from a time- and voltage-dependent reduction of K_{ACh} current which results from Ca^{2+} entry and Ca^{2+}–CaM stimulation of RGS proteins which accelerate the GTPase activity of the GPCR (Ishii *et al.* 2001, 2002). One characteristic of relaxation is voltage dependence: more of the K_{ACh} current shows relaxation as the prepulse is depolarized. Another characteristic is that relaxation is reduced as $[ACh]_0$ is increased. GTPγS, a non-hydrolysable GTP analogue, also abolished the relaxation behaviour. The time-dependent current change in GTPγS-loaded atrial cells represented the intrinsic gating of K_{ACh} channels.

To extract the character of relaxation, the experimental currents showing relaxation with 0.1 and 0.3 μM ACh were normalized to that evoked by GTPγS (figure 3*c*(i)). The equivalent simulated K_{ACh} currents using the improved integrated model are shown in figure 3*c*(ii). The relaxation is generated by the voltage-dependent facilitation of GTPase activity of $G_{K\alpha}$ due to RGSs. Therefore, we incorporated this process in k_6 of the G_K protein cycle model by formulating k_6 as a function of the membrane potential (table 1, k_6; see §2 for